GRADIENT STEP DENOISER FOR CONVERGENT PLUG-AND-PLAY

Anonymous authors
Paper under double-blind review

ABSTRACT

Plug-and-Play (PnP) methods constitute a class of iterative algorithms for imaging problems where regularization is performed by an off-the-shelf denoiser. Although PnP methods can lead to tremendous visual performance for various image problems, the few existing convergence guarantees are based on unrealistic (or suboptimal) hypotheses on the denoiser, or limited to strongly convex data-fidelity terms. We propose a new type of PnP method, based on half-quadratic splitting, for which the denoiser is realized as a gradient descent step on a functional parameterized by a deep neural network. Exploiting convergence results for proximal gradient descent algorithms in the non-convex setting, we show that the proposed PnP algorithm is a convergent iterative scheme that targets stationary points of an explicit global functional. Besides, experiments show that it is possible to learn such a deep denoiser while not compromising the performance in comparison to other state-of-the-art deep denoisers used in PnP schemes. We apply our proximal gradient algorithm to various ill-posed inverse problems, e.g. deblurring, super-resolution and inpainting. For all these applications, numerical results empirically confirm the convergence results. Experiments also show that this new algorithm reaches state-of-the-art performance, both quantitatively and qualitatively.

1 INTRODUCTION

Image restoration (IR) problems can be formulated as inverse problems of the form

$$x^* \in \arg\min_x f(x) + \lambda g(x) \tag{1}$$

where f is a term measuring the fidelity to a degraded observation y, and g is a regularization term weighted by a parameter $\lambda \geq 0$. Generally, the degradation of a clean image $\hat{x}$ can be modeled by a linear operation $y = A\hat{x} + \xi$, where A is a degradation matrix and ξ a white Gaussian noise. In this context, the maximum a posteriori (MAP) derivation relates the data-fidelity term to the likelihood $f(x) = -\log p(y|x) = \frac{1}{2\sigma^2}||Ax - y||^2$, while the regularization term is related to the chosen prior.

Regularization is crucial since it tackles the ill-posedness of the IR task by bringing a priori knowledge on the solution. A lot of research has been dedicated to designing accurate priors g. Among the most classical priors, one can single out total variation (Rudin et al., 1992), wavelet sparsity (Mallat, 2009) or patch-based Gaussian mixtures (Zoran & Weiss, 2011). Designing a relevant prior g is a difficult task and recent approaches rather apply deep learning techniques to directly learn a prior from a database of clean images (Lunz et al., 2018; Prost et al., 2021; González et al., 2021).

Generally, the problem (1) does not have a closed-form solution, and an optimization algorithm is required. First-order proximal splitting algorithms (Combettes & Pesquet, 2011) operate individually on f and g via the proximity operator

$$\mathrm{Prox}_f(x) = \arg\min_z \frac{1}{2}||x - z||^2 + f(z) \tag{2}$$

Among them, half-quadratic splitting (HQS) (Geman & Yang, 1995) alternately applies the proximal operators of f and g. Proximal methods are particularly useful when either f or g is nonsmooth.

Plug-and-Play (PnP) methods (Venkatakrishnan et al., 2013) build on proximal splitting algorithms by replacing the proximity operator of g with a generic denoiser, *e.g.* a pretrained deep network.

These methods achieve state-of-the-art results (Buzzard et al., 2018; Ahmad et al., 2020; Yuan et al., 2020; Zhang et al., 2021) in various IR problems. However, since a generic denoiser cannot generally be expressed as a proximal mapping (Moreau, 1965), convergence results, which stem from the properties of the proximal operator, are difficult to obtain. Moreover, the regularizer g is only made implicit via the denoising operation. Therefore, PnP algorithms do not seek the minimization of an explicit objective functional which strongly limits their interpretation and numerical control.

In order to keep tractability of a minimization problem, Romano et al. (2017) proposed, with regularization by denoising (RED), an explicit prior g that exploits a given generic denoiser D in the form $g(x) = \frac{1}{2}\langle x, x - D(x)\rangle$. With strong assumptions on the denoiser (in particular a symmetric Jacobian assumption), they show that it verifies

$$\nabla_x g(x) = x - D(x). \tag{3}$$

Such a denoiser is then plugged in gradient-based minimization schemes. Despite having shown very good results on various image restoration tasks, as later pointed out by Reehorst & Schniter (2018) or Saremi (2019), existing deep denoisers lack Jacobian symmetry. Hence, RED does not minimize an explicit functional and is not guaranteed to converge.

Contributions. In this work, we develop a PnP scheme with novel theoretical convergence guarantees and state-of-the-art IR performance. Departing from the PnP-HQS framework, we plug a denoiser that inherently satisfies equation (3) without sacrificing the denoising performance. The resulting fixed-point algorithm is guaranteed to converge to a stationary point of an explicit functional. This convergence guarantee does not require strong convexity of the data-fidelity term, thus encompassing ill-posed IR tasks like deblurring, super-resolution or inpainting.

2 Related works

PnP methods have been successfully applied in the literature with various splitting schemes: HQS (Zhang et al., 2017b; 2021), ADMM (Romano et al., 2017; Ryu et al., 2019), Proximal Gradient Descent (PGD) (Terris et al., 2020). First used with classical non deep denoisers such as BM3D (Chan et al., 2016) and pseudo-linear denoisers (Nair et al., 2021; Gavaskar et al., 2021), more recent PnP approaches (Meinhardt et al., 2017; Ryu et al., 2019) rely on efficient off-the-shelf deep denoisers such as DnCNN (Zhang et al., 2017a). State-of-the-art IR results are currently obtained with denoisers that are specifically designed to be integrated in PnP schemes, like IRCNN (Zhang et al., 2017b) or DRUNET (Zhang et al., 2021). Though providing excellent restorations, such schemes are not guaranteed to converge for all kinds of denoisers or IR tasks.

Designing convergence proofs for PnP algorithms is an active research topic. Sreehari et al. (2016) first used the proximal theorem of Moreau (Moreau, 1965) to give sufficient conditions for the denoiser to be an explicit proximal map, which are applied to a pseudo-linear denoiser. The convergence with pseudo-linear denoisers have then been extensively studied (Gavaskar & Chaudhury, 2020; Nair et al., 2021; Chan, 2019). However, in the PnP literature, state-of-the-art results are obtained with deep denoisers. Various assumptions have been proposed to ensure the convergence of the related PnP schemes. With a "bounded denoiser" assumption, Chan et al. (2016); Gavaskar & Chaudhury (2019) first showed convergence of PnP-ADMM with stepsizes decreasing to 0. Cohen et al. (2021) considers the wider class of demi-contractive mappings, but this condition is hard to verify in practice. Many works focus on the Lipschitz properties of the PnP operator, in order to rely on Banach fixed-point theorem. Depending on the splitting algorithm in use, convergence can then be obtained by assuming the denoiser averaged (Sun et al., 2019), firmly nonexpansive (Sun et al., 2021; Terris et al., 2020) or simply a nonexpansive (Reehorst & Schniter, 2018; Liu et al., 2021). These settings are unrealistic as deep denoisers do not generally satisfy such properties. Methods like Ryu et al. (2019) or Terris et al. (2020) thus propose different ways to train deep denoisers with constrained Lipschitz constants in order to fit the technical properties required for convergence. But imposing hard Lipschitz constraints on the network alters its denoising performance (Bohra et al., 2021; Hertrich et al., 2021). Yet, Ryu et al. (2019) manages to get a convergent PnP scheme without assuming the nonexpansiveness of D. This comes at the cost of imposing strong convexity on the data-fidelity term f, which excludes many IR tasks like deblurring, super-resolution and inpainting. As a matter of fact, given the ill-posedness of IR problems, looking for a unique solution via contractive operators is a restrictive assumption. In this work, we do not impose contractiveness, but still obtain convergence results with realistic hypotheses.

One can relate the ideal deep denoiser to the "true" natural image prior p via Tweedie's Identity. In (Efron, 2011), it is indeed shown that the Minimum Mean Square Error (MMSE) denoiser D_σ^* (at noise level σ) verifies $D_\sigma(x) = x + \sigma^2 \nabla_x \log p_\sigma(x)$ where p_σ is the convolution of p with the density of $\mathcal{N}(0, \sigma^2 \operatorname{Id})$. In a recent line of research (Bigdeli et al., 2017; Xu et al., 2020; Laumont et al., 2021; Kadkhodaie & Simoncelli, 2020), this relation is used to plug a denoiser in gradient-based dynamics. In practice, the MMSE denoiser cannot be computed explicitly and Tweedie's Identity does not hold for deep approximations of the MMSE. Finally, let us mention that the form of prior considered here was already suggested in Bigdeli & Zwicker (2017) and Romano et al. (2017, Section 5.2) but not exploited for convergence analysis.

3 The Gradient Step Plug-and-Play

The proposed method is based on the PnP version of half-quadratic-splitting (PnP-HQS) that amounts to replacing the proximity operator of the prior g with an off-the-shelf denoiser D_σ. In order to define a convergent PnP scheme, we first set up in Section 3.1 a Gradient Step (GS) denoiser. We then introduce the Gradient Step PnP algorithm in Section 3.2.

3.1 Gradient Step denoiser

We propose to plug a denoising operator D_σ that takes the form of a gradient descent step

$$D_\sigma = \operatorname{Id} - \nabla g_\sigma, \tag{4}$$

with $g_\sigma : \mathbb{R}^n \to \mathbb{R}$. Contrary to Romano et al. (2017), our denoiser exactly represents a conservative vector field. The choice of the parameterization of g_σ is fundamental for the denoising performance. As already noticed in Salimans & Ho (2021), we experimentally found that directly modeling g_σ as a neural network (*e.g.* a standard network used for classification) leads to poor denoising performance. In order to keep the strength of state-of-the-art unconstrained denoisers, we rather use

$$g_\sigma(x) = \frac{1}{2}||x - N_\sigma(x)||^2 \tag{5}$$

where $N_\sigma : \mathbb{R}^n \to \mathbb{R}^n$ is parameterized by a neural network. The resulting denoising operator is

$$D_\sigma(x) = x - \nabla g_\sigma(x) = N_\sigma(x) + J_{N_\sigma}(x)^T (x - N_\sigma(x)), \tag{6}$$

where $J_{N_\sigma}(x)$ refers to the Jacobian of N_σ at point x. Let us highlight that, thanks to this definition of D_σ, **we can parameterize N_σ with any differentiable neural network architecture** $\mathbb{R}^n \to \mathbb{R}^n$ that has proven efficient for image denoising. Although the representation power of the denoiser is limited by the particular form (6), we show (see Section 5.1) that such parameterization still yields state-of-the-art denoising results.

We train the denoiser D_σ by minimizing the MSE loss function

$$D_\sigma \longmapsto \mathbb{E}_{x \sim p, \xi_\sigma \sim \mathcal{N}(0, \sigma^2 I)}[||D_\sigma(x + \xi_\sigma) - x||^2]. \tag{7}$$

Using equation (4), it can be written in terms of g_σ:

$$\mathcal{L}(g_\sigma) = \mathbb{E}_{x \sim p, \xi_\sigma \sim \mathcal{N}(0, \sigma^2 I)}[||\nabla g_\sigma(x + \xi_\sigma) - \xi_\sigma||^2]. \tag{8}$$

Remark 1. *By definition, the optimal solution $g_\sigma^* \in \arg\min \mathcal{L}$ is related to the MMSE denoiser D_σ^*, that is, the best non-linear predictor of x given $x + \xi_\sigma$. Therefore, it satisfies Tweedie's formula and $\nabla g_\sigma^* = -\sigma^2 \nabla \log p_\sigma$ (Efron, 2011)* i.e. *$g_\sigma^* = -\sigma^2 \log p_\sigma + C$, for some $C \in \mathbb{R}$. Hence approximating the MMSE denoiser with a denoiser parameterized as (4) is related to approximating the logarithm of the smoothed image prior p_σ with $-\frac{1}{\sigma^2} g_\sigma$. This relation was used for image generation in the context of "Denoising Score Matching" by Saremi & Hyvarinen (2019); Bigdeli et al. (2020).*

3.2 A Plug-and-Play method for explicit minimization

The standard PnP-HQS operator is $T_{\text{PnP-HQS}} = D_\sigma \circ \operatorname{Prox}_{\tau f}$, *i.e.* $(\operatorname{Id} - \nabla g_\sigma) \circ \operatorname{Prox}_{\tau f}$ when using the GS denoiser as D_σ. For convergence analysis, it proves fruitful to fit the proximal gradient descent algorithm by switching the proximal and gradient steps. We also propose to relax the denoising step with a parameter $\lambda \geq 0$. Our PnP algorithm with GS denoiser (GS-PnP) then writes

$$\begin{aligned} x_{k+1} = T_{\text{GS-PnP}}^{\tau,\lambda}(x_k) \text{ with } T_{\text{GS-PnP}}^{\tau,\lambda} &= \operatorname{Prox}_{\tau f} \circ (\tau \lambda D_\sigma + (1 - \tau\lambda) \operatorname{Id}), \\ &= \operatorname{Prox}_{\tau f} \circ (\operatorname{Id} - \tau \lambda \nabla g_\sigma). \end{aligned} \tag{9}$$

Under suitable conditions on f and g_σ (see Lemma 1 in Appendix A), fixed points of the operator $T^{\tau,\lambda}_{\text{GS-PnP}}$ correspond to critical points of

$$F(x) = f(x) + \lambda g_\sigma(x). \tag{10}$$

Therefore, using the GS denoiser from equation (4) is equivalent to include an explicit regularization and thus leads to a tractable global optimization problem solved by the PnP algorithm. Our complete PnP scheme is presented in Algorithm 1. It includes a backtracking procedure that will be detailed in Section 4.2. Also, after convergence, we found it useful to apply an extra gradient step $\mathrm{Id} - \lambda\tau\nabla g_\sigma$ in order to discard the residual noise brought by the last proximal step $\mathrm{Prox}_{\tau f}$.

4 Convergence analysis

In this section, we introduce conditions on f and D_σ that will ensure the convergence of the PnP iterations (9) towards a solution of (10). For that purpose, we make use of the literature of convergence analysis (Attouch et al., 2013; Beck, 2017; Beck & Teboulle, 2009; Gu et al., 2018) of the proximal gradient descent algorithm in the non-convex setting.

Algorithm 1: Plug-and-Play image restoration

Param.: init. z_0, $\lambda > 0$, $\sigma \geq 0$, $\epsilon > 0$, $\tau_0 > 0$, $K \in \mathbb{N}^*$, $\eta \in (0,1)$, $\gamma \in (0, 1/2)$.
Input : degraded image y.
Output: restored image $\hat{x}$.
$k = 0$; $x_0 = \mathrm{Prox}_{\tau f}(z_0)$; $\tau = \tau_0/\eta$; $\texttt{dif} > \epsilon$;
while $k < K$ *and* $\texttt{dif} > \epsilon$ **do**
  $z_k = \lambda\tau D_\sigma(x_k) + (1-\lambda\tau)x_k$;
  $x_{k+1} = \mathrm{Prox}_{\tau f}(z_k)$;
  if $F(x_k) - F(x_{k+1}) < \frac{\gamma}{\tau}||x_k - x_{k+1}||^2$;
  then $\tau = \eta\tau$;
  else $\texttt{dif} = \frac{F(x_k)-F(x_{k+1})}{F(x_0)}$; $k = k+1$;
end
$\hat{x} = \lambda\tau D_\sigma(x_K) + (1-\lambda\tau)x_K$;

4.1 Convergence results

A common setting for image restoration is the convex smooth L^2 data-fidelity $f(x) = ||Ax - y||^2$. In order to cover the noiseless case or to deal with a broader range of degradation models, like Laplace or Poisson noise, we only assume f to be proper, lower semicontinous and convex. On the other hand, the regularizer g_σ is assumed to be differentiable with Lipschitz gradient, but not necessarily convex. Without further assumptions on f and g_σ, the following theorem establishes the convergence of the objective function values and convergence of the residual.

Theorem 1 (Proof in Appendix A)**.** *Let $f : \mathbb{R}^n \to \mathbb{R} \cup \{+\infty\}$ and $g_\sigma : \mathbb{R}^n \to \mathbb{R}$ be proper lower semicontinous functions with f convex and g_σ differentiable with L-Lipschitz gradient. Let $\lambda > 0$, $F = f + \lambda g_\sigma$ and assume that F is bounded from below. Then, for $\tau < \frac{1}{\lambda L}$, the iterates x_k given by the iterative scheme (9) verify*

(i) $(F(x_k))$ is non-increasing and converges.

(ii) The residual $||x_{k+1} - x_k||$ converges to 0.

(iii) All cluster points of the sequence (x_k) are stationary points of (10).

Remark 2. *In the non-convex setting, the quantity $\gamma_k = \min_{0\leq i\leq k} ||x_{i+1} - x_i||^2$ is commonly used to analyze the convergence rate of the algorithm (Beck & Teboulle, 2009; Ochs et al., 2014). Following the proof of Theorem 1 in Appendix A, we can obtain $\gamma_k \leq \frac{1}{k}\frac{F(x_0)-\lim F(x_k)}{\frac{1}{2\tau}-\frac{L}{2}}$ that is to say a $\mathcal{O}(\frac{1}{k})$ convergence rate for the squared L^2 residual.*

Remark 3. *Even if most data-fidelity terms f encountered in image restoration are convex, Theorem 1 can be extended to nonconvex f. The proof of (iii) requires technical adaptations that can be found in (Li & Lin, 2015, Theorem 1) (in particular the 1-Lipschitz property of $\mathrm{Prox}_{\tau f}$ does not hold anymore).*

We can further obtain convergence of the iterates by assuming that the generated sequence (x_k) is bounded and that f and g_σ verify the Kurdyka-Lojasiewicz (KL) property. The boundedness of (x_k) is discussed in Appendix B. The KL property (defined in Appendix C) has been widely used to study the convergence of optimization algorithms in the non-convex setting (Attouch et al., 2010; 2013; Ochs et al., 2014). Very large classes of functions, in particular all the semi-algebraic functions, satisfy this property. In practice, in the extent of our analysis, the KL property is always satisfied.

Theorem 2 (Proof in Attouch et al. (2013), Theorem 5.1)**.** *Let $f : \mathbb{R}^n \to \mathbb{R} \cup \{+\infty\}$ and $g_\sigma : \mathbb{R}^n \to \mathbb{R}$ be proper lower semicontinous functions with f convex and g_σ differentiable with L-Lipschitz gradient. Let $\lambda > 0$, $F = f + \lambda g_\sigma$ and assume that F is bounded from below. Assume that F verify the KL property. Suppose that $\tau < \frac{1}{\lambda L}$. If the sequence (x_k) given by the iterative scheme (9) is bounded, then it converges, with finite length, to a critical point x^* of F.*

Remark 4. *As explained in Attouch et al. (2013, Remark 5.2), the continuity of f is not required since we use the "exact forward-backward splitting algorithm". We can thus deal with non-continuous data-fidelity terms, as it is the case with the inpainting application in Appendix G.4.*

As detailed before, the assumptions in Theorems 1 and 2 on f and g_σ are reasonable from a practical perspective. Indeed, using a network N_σ with differentiable activation functions, the function g_σ introduced in Section 3 is differentiable with Lipschitz gradient (details and proof are given in Appendix D). Therefore, for a large variety of image restoration tasks, our PnP scheme (9) is guaranteed to converge to a stationary point of the targeted objective function F.

4.2 Backtracking to handle the Lipschitz constant of ∇g_σ

The convergence of Algorithm 1 actually requires to control the Lipschitz constant of ∇g_σ only on a small subset of images related to $\{x_k\}$. Therefore, estimating L for all images and setting the maximum stepsize τ accordingly will lead to sub-optimal convergence speed. In order to avoid small stepsizes, we use the backtracking strategy (Beck, 2017, Chapter 10).

The convergence study in the proof of Theorem 1 is based on the sufficient decrease property of F established equation (22). Without knowing the exact Lipschitz constant L, backtracking aims at finding the maximal stepsize τ that yields the sufficient decrease property. Given $\gamma \in (0, 1/2)$, $\eta \in [0, 1)$ and an initial stepsize $\tau_0 > 0$, the backtracking procedure consists in applying at each iteration k the following update rule on τ:

$$\text{while} \quad F(x_k) - F(T^{\tau,\lambda}_{\text{GS-PnP}}(x_k)) < \frac{\gamma}{\tau}||T^{\tau,\lambda}_{\text{GS-PnP}}(x_k) - x_k||^2, \quad \tau \longleftarrow \eta\tau. \tag{11}$$

Proposition 1 (Proof in Appendix E)**.** *Under the assumptions of Theorem 1, at each iteration of the algorithm, the backtracking procedure (11) is finite (*i.e. *a stepsize satifying $F(x_k) - F(T^{\tau,\lambda}_{GS\text{-}PnP}(x_k)) \geq \frac{\gamma}{\tau}||T^{\tau,\lambda}_{GS\text{-}PnP}(x_k) - x_k||^2$ is found in a finite number if iterations), and with backtracking, the convergence results of Theorem 1 and Theorem 2 still hold.*

Remark 5. *In practice, as explained in Section 5, we choose to initialize the stepsize as $\lambda\tau_0 = 1$ and backtracking hardly ever activates. In this particular case, our results prove convergence of the standard PnP-HQS scheme $x_{k+1} = \text{Prox}_{\tau f} \circ D_\sigma(x_k)$ applied with our specific denoiser.*

5 Experiments

5.1 Gradient-descent-based denoiser

Denoising Network Architecture We choose to parameterize N_σ with the architecture DRUNet (Zhang et al., 2021)) (represented in Appendix H), a U-Net in which residual blocks are integrated. One first benefit of DRUNet is that it is built to take the noise level σ as input, which is consistent with our formulation. Also, the U-Net models have previously offered good results in the context of prior approximation via Denoising Score Matching (Ho et al., 2020). Furthermore, Zhang et al. (2021) showed that DRUNet yields state-of-the-art results for denoising but also for PnP image restoration. In order to ensure differentiability w.r.t the input, we change RELU activations to ELU. We also limit the number of residual blocks to 2 at each scale to lower the computational burden.

Training details We use the color image training dataset proposed in Zhang et al. (2021) *i.e.* a combination of the Berkeley segmentation dataset (CBSD) (Martin et al., 2001), Waterloo Exploration Database (Ma et al., 2017), DIV2K dataset (Agustsson & Timofte, 2017) and Flick2K dataset (Lim et al., 2017). During training, the input images are corrupted with a white Gaussian noise ξ_σ with standard deviation σ randomly chosen in $[0, 50/255]$. With our parameterization (6) of D_σ, the network N_σ is trained to minimize the L^2 loss (7). While the original DRUNet is trained with L^1 loss, we stick to the L^2 loss to keep the interpretability of g_σ as an approximation of the log prior (see Remark 1). For each batch, the gradient ∇g_σ is computed with PyTorch differentiation

tools. We train the model on 128×128 patches randomly sampled from the training images, with batch size 16, during 1500 epochs. We use the ADAM optimizer with learning rate 10^{-4}, divided by 2 every 300 epochs. It takes around one week to train the model on a single Tesla P100 GPU.

Denoising results We evaluate the PSNR performance of the proposed GS denoiser (GS-DRUNet) on 256×256 color images center-cropped from the original CBSD68 dataset images (Martin et al., 2001). In Table 1, we compare, for various noise levels σ, our model with the simplified DRUNet (called "DRUNet *light*") that has the same architecture as our GS-DRUNet (2 residual blocks) and that is trained (with L^2 loss) without the conservative field constraint. We also provide comparisons with the original DRUNet (Zhang et al., 2021) (with 4 residual blocks at each scale and trained with L^1 loss) and two state-of-the-art denoisers encountered in the PnP literature: FFDNet (Zhang et al., 2018) and DnCNN (Zhang et al., 2017a). For each network, we indicate in Table 1 the average runtime while processing a 256×256 color image on one Tesla P100 GPU.

Our GS-DRUNet denoiser, despite being constrained to be an exact conservative field, reaches the performance of (and even slightly outperforms) its unconstrained counterpart DRUNet *light*. Second, departing from the latter, we are able to reduce the processing time by a large margin ($\div 7$) while keeping close PSNR to the original DRUNet (around -0.05dB) and maintaining a significant PSNR gap (around +0.5dB) with other deep denoisers like DnCNN and FFDNet. Note that the time difference between GS-DRUNet and DRUNet *light* is due to the computation of ∇g_σ via backpropagation. These results indicate that GS-DRUNet is likely to yield a competitive and fast PnP algorithm.

$\sigma(./255)$	5	15	25	50	Time (ms)
FFDNet	39.95	33.53	30.84	27.54	1.9
DnCNN	39.80	33.55	30.87	27.52	2.3
DRUNet	**40.31**	**33.97**	**31.32**	**28.08**	69.8
DRUNet *light*	40.19	33.89	31.25	28.00	6.3
GS-DRUNet	<u>40.26</u>	<u>33.90</u>	<u>31.26</u>	<u>28.01</u>	10.4

Table 1: Average PSNR denoising performance and runtime of our GS denoiser on 256×256 center-cropped images from the CBSD68 dataset, for various noise levels σ. While keeping small runtime, GS-DRUNet slightly outperforms its unconstrained counterpart DRUNet *light* and outdistances the deep denoisers FFDNet and DnCNN.

5.2 Plug-and-Play image restoration

We apply our PnP Algorithm 1 to deblurring in Section 5.2.1, super-resolution in Section 5.2.2 and inpainting in Appendix G.4. In all cases, we seek an estimate $x \in \mathbb{R}^n$ of the original clean image $\hat{x} \in \mathbb{R}^n$, from an observation $y \in \mathbb{R}^m$ obtained as $y = A\hat{x} + \xi_\nu$, with A a $m \times n$ degradation matrix and ξ_ν a white Gaussian noise with zero mean and standard deviation ν. The objective function minimized by Algorithm 1 is

$$F(x) = \frac{1}{2\nu^2}||Ax - y||^2 + \frac{\lambda}{2}||N_\sigma(x) - x||^2. \tag{12}$$

In practice, for $\nu > 0$, we multiply F in equation (12) by ν^2 and consider $F = f + \lambda_\nu g_\sigma$ with $f(x) = \frac{1}{2}||Ax - y||^2$, $g_\sigma(x) = \frac{1}{2}||N_\sigma(x) - x||^2$ and $\lambda_\nu = \lambda\nu^2$. With this formulation, the convergences of iterates and objective values are guaranteed by Theorems 1 and 2. We demonstrate in Appendix G.4 that our framework can be extended to other kinds of objective functions. For example, inpainting noise-free input images leads to a non differentiable data-fidelity term f.

Due to the large computational time of some compared methods, we use for evaluation and comparison a subset of 10 color images taken from the CBSD68 dataset (CBSD10) together with the three famous set3C images (butterfly, leaves and starfish). Quantitative results run on the full CBSD68 dataset are also given in Appendix G. All input images are center-cropped to the size 256×256. For each IR problem, we provide default values for the parameters σ and λ that can be used to treat successfully a large class of images and degradations. The influence of both parameters is analyzed in Appendix G.5. Performance could be marginally improved by tuning λ for each image, for example with the method of Wei et al. (2020) based on reinforcement learning. In all our experiments, backtracking is performed with $\eta = 0.9$ and $\gamma = 0.1$. We estimated (see Appendix D) that on a majority of images, the Lipschitz constant L of ∇g_σ is slightly larger than 1. As convergence is ensured for $\lambda_\nu \tau = \nu^2 \lambda \tau < L$, we choose to set the initial stepsize to $\tau_0 = (\nu^2\lambda)^{-1}$. At the first iteration, the gradient step in equation (9) is thus exactly D_σ. We observe that in the majority of our experiments, backtracking is never activated. Finally, the algorithm is initialized with a proximal step and terminates when the relative difference between two consecutive values of the objective function is less than ϵ or the number of iterations exceeds K.

5.2.1 DEBLURRING

For image deblurring, the degradation operator $A = H$ is a convolution performed with circular boundary conditions. Therefore, $H = \mathcal{F}^* \Lambda \mathcal{F}$, where $\mathcal{F}$ is the orthogonal matrix of the discrete Fourier transform (and $\mathcal{F}^*$ its inverse), and Λ is a diagonal matrix. The proximal operator of the data-fidelity term $f(x) = \frac{1}{2}||Hx - y||^2$ involves only element-wise inversion and writes

$$\mathrm{Prox}_{\tau f}(z) = \mathcal{F}^*(I_n + \tau \Lambda^* \Lambda)^{-1} \mathcal{F}(\tau H^T y + z). \tag{13}$$

We demonstrate the effectiveness of our method on a large variety of blur kernels (represented in Table 2) and noise levels. As in Zhang et al. (2017b); Pesquet et al. (2021); Zhang et al. (2021), we use the 8 real-world camera shake kernels proposed in Levin et al. (2009) as well as the 9×9 uniform kernel and the 25×25 Gaussian kernel with standard deviation 1.6 (as in Romano et al. (2017)). We consider Gaussian noise with 3 noise levels $\nu \in \{2.55, 7.65, 12.75\}/255$ *i.e.* $\nu \in \{0.01, 0.03, 0.05\}$. For all noise levels, we set $\sigma = 1.8\nu$, $\lambda_\nu = \nu^2 \lambda = 0.1$ for motion blur (kernels (a) to (h)) and $\lambda_\nu = 0.075$ for static blur (kernels (i) and (j)). Initialization is done with $z_0 = y$ but we show in Appendix G.6 the robustness to the initialization. The stopping criteria are $\epsilon = 10^{-5}$ and $K = 400$.

We compare in Table 2 our method (GS-PnP) against the patch-based method EPLL (Zoran & Weiss, 2011; Hurault et al., 2018), the deep PnP methods IRCNN (Zhang et al., 2017b), DPIR (Zhang et al., 2021), MMO (Pesquet et al., 2021), and the "RED-FP" algorithm (Romano et al., 2017) (with TNRD denoiser (Chen & Pock, 2016)) referred to as RED. Both IRCNN and DPIR use PnP-HQS with a fast decrease of τ and σ in a few iterations (8 iterations for DPIR) without guarantee of convergence. DPIR uses the DRUNet denoiser from Table 1. MMO is the only compared method that guarantees convergence by plugging a DnCNN denoiser trained with Lipschitz constraints, but the only pretrained network given is for very low noise level. Finally, as RED only treats the Y channel in the YCbCr color space, we also indicate in Appendix G.2, for RED and the proposed method, the PSNR evaluated on the Y channel only.

Among all methods, GS-PnP closely follows DPIR in terms of PSNR for low noise level but performs equally or better for higher noise levels. Other comparisons are conducted in Appendix G.2 on the Set3c dataset (Table 4) and on the full CBSD68 dataset (Table 5). These results all confirm that GS-PnP reaches state-of-the-art in PnP deblurring, for a variety of kernels and noise levels.

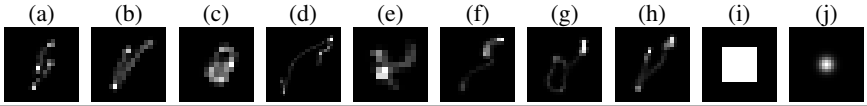

ν	Method	(a)	(b)	(c)	(d)	(e)	(f)	(g)	(h)	(i)	(j)	*Avg*
0.01	EPLL	28.32	28.24	28.36	25.80	29.61	27.15	26.90	26.69	25.84	26.49	*27.34*
	RED	30.47	30.01	30.29	28.09	31.22	28.92	28.90	28.67	26.66	28.45	*29.17*
	IRCNN	32.96	32.62	32.53	32.44	33.51	33.62	32.54	32.20	28.11	29.19	*31.97*
	MMO	32.35	32.06	32.24	31.67	31.77	33.17	32.30	31.80	27.81	**29.26**	*31.44*
	DPIR	**33.76**	**33.30**	**33.04**	**33.09**	**34.10**	**34.34**	**33.06**	**32.77**	**28.34**	29.16	***32.50***
	GS-PnP	33.52	33.07	32.91	32.83	34.07	34.25	32.96	32.54	28.11	29.03	*32.33*
0.03	EPLL	25.31	25.12	25.82	23.75	26.99	25.23	25.00	24.59	24.34	25.43	*25.16*
	RED	25.71	25.32	25.71	24.38	26.65	25.50	25.27	24.99	23.51	25.54	*25.26*
	IRCNN	28.96	28.65	28.90	28.38	30.03	29.87	28.92	28.52	25.92	27.64	*28.58*
	DPIR	**29.38**	**29.06**	**29.21**	**28.77**	30.22	**30.23**	**29.34**	28.90	26.19	27.81	***28.91***
	GS-PnP	29.22	28.89	29.20	28.60	**30.32**	30.21	29.32	**28.92**	**26.38**	**27.89**	*28.90*
0.05	EPLL	24.08	23.91	24.78	22.57	25.68	23.98	23.70	23.19	23.75	24.78	*24.04*
	RED	22.78	22.54	23.13	21.92	23.78	22.97	22.89	22.67	22.01	23.78	*22.84*
	IRCNN	27.00	26.74	27.25	26.37	28.29	28.06	27.22	26.81	24.85	26.83	*26.94*
	DPIR	**27.52**	**27.35**	**27.73**	**27.02**	28.63	**28.46**	27.79	27.30	25.25	27.11	*27.42*
	GS-PnP	27.45	27.28	27.70	26.98	**28.68**	28.44	**27.81**	**27.38**	**25.49**	**27.15**	***27.44***

Table 2: PSNR(dB) comparison of image deblurring methods on CBSD10 with various blur kernels k and noise levels ν. Best and second best results are displayed in bold and underlined.

For qualitative comparison, we show in Figure 1(c-f) the deblurring obtained with various methods on the image "starfish" (from set3C). Note that our algorithm, compared to competing methods, can recover the sharpest edges. We also give convergence curves that empirically confirm the convergence of the values $F(x_k)$ (g) and of the residual $\min_{0 \leq i \leq k} ||x_{i+1} - x_i||^2 / ||x_0||^2$ (h). These observations are supported by the additional experiment shown in Appendix G.2, Figure 6.

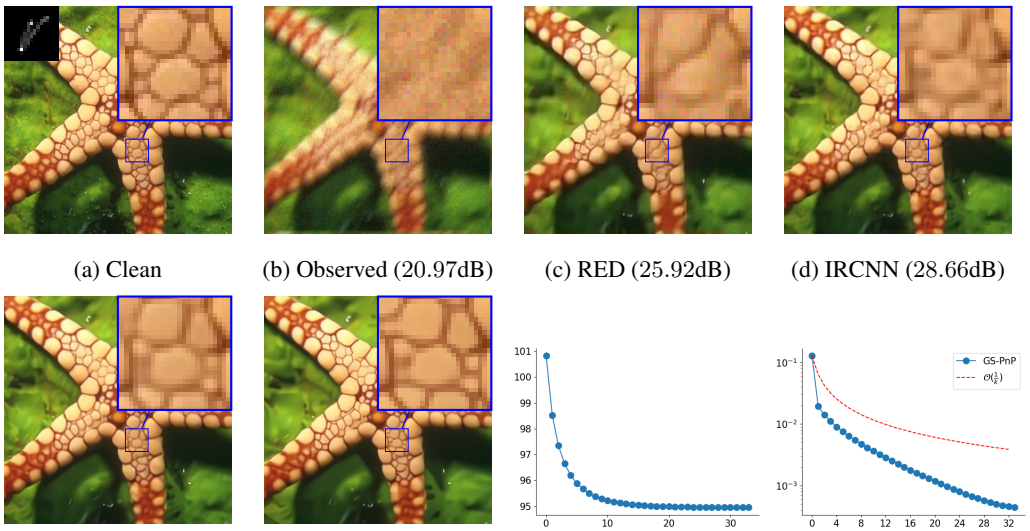

(a) Clean (b) Observed (20.97dB) (c) RED (25.92dB) (d) IRCNN (28.66dB)

(e) DPIR (29.76dB) (f) GS-PnP (29.89dB) (g) $F(x_k)$ (h) γ_k (log scale)

Figure 1: Deblurring with various methods of "starfish" degraded with the indicated blur kernel and input noise level $\nu = 0.03$. Note that our algorithm better recovers the structures. In (g) and (h), we show the evolution of $F(x_k)$ and $\gamma_k = \min_{0 \leq i \leq k} ||x_{i+1} - x_i||^2 / ||x_0||^2$ and in Appendix G.1 the evolution of the PSNR. We empirically verify convergence of functional values and residual. Note that the empirical convergence rate is (h) is faster than the $\mathcal{O}(\frac{1}{k})$ theoretical worst case rate established in Remark 2.

5.2.2 SUPER-RESOLUTION

For single image super-resolution, the low-resolution image $y \in \mathbb{R}^m$ is obtained from the high-resolution one $x \in \mathbb{R}^n$ via $y = SHx + \xi_\nu$ where $H \in \mathbb{R}^{n \times n}$ is the convolution with anti-aliasing kernel. The matrix S is the standard s-fold downsampling matrix of size $m \times n$ and $n = s^2 \times m$. In this context, we make use of the closed-form calculation of the proximal map for the data-fidelity term $f(x) = \frac{1}{2}||SHx - y||^2$, given by Zhao et al. (2016):

$$\text{Prox}_{\tau f}(z) = \hat{z}_\tau - \frac{1}{s^2} \mathcal{F}^* \underline{\Lambda}^* \left(I_m + \frac{\tau}{s^2} \underline{\Lambda} \underline{\Lambda}^* \right)^{-1} \underline{\Lambda} \mathcal{F} \hat{z}_\tau, \tag{14}$$

where $\hat{z}_\tau = \tau H^T S^T y + z$ and $\underline{\Lambda} = [\Lambda_1, \ldots, \Lambda_{s^2}] \in \mathbb{R}^{m \times n}$, with $\Lambda = \text{diag}(\Lambda_1, \ldots, \Lambda_{s^2})$ a block-diagonal decomposition according to a $s \times s$ paving of the Fourier domain. Note that $I_m + \frac{\tau}{d} \underline{\Lambda} \underline{\Lambda}^*$ is a $m \times m$ diagonal matrix and its inverse is computed element-wise. As expected, with $s = 1$, equation (14) comes down to equation (13).

As in Zhang et al. (2021), we evaluate super-resolution performance on 8 Gaussian blur kernels represented in Table 3: 4 isotropic kernels with different standard deviations (0.7, 1.2, 1.6 and 2.0) and 4 anisotropic kernels. Results are averaged between isotropic and anisotropic. We consider downsampled images at scale $s = 2$ and $s = 3$ and Gaussian noise with 3 different noise levels $\nu \in \{0.01, 0.03, 0.05\}$. Our method (GS-PnP) is compared against bicubic upsampling, RED, IRCNN ("IRCNN+" from Zhang et al. (2021)) and DPIR. We give again in Appendix G.3 the results obtained on the Set3C dataset (Table 7). All our results are obtained with $\lambda_\nu = \nu^2 \lambda = 0.065$ and $\sigma = 2\nu$. Initialization z_0 is done with a bicubic interpolation of y (with a shift correction (Zhang et al., 2021)) and the stopping criteria are $\epsilon = 10^{-6}$ and $K = 400$.

Our method outperforms in PSNR all other PnP methods over the considered range of blur kernels, noise levels and scale factors. We show in Figure 2 the super-resolution of the image "leaves" downsampled by 2, with an isotropic kernel and noise level $\nu = 0.03$. GS-PnP (f) recovers more accurately structures and color details than competing approaches (c-e), while converging in terms of function values (g) and residual (h). Additional visual comparisons are presented in Appendix G.3.

Kernels	Method	$s=2$			$s=3$			*Avg*
		$\nu=0.01$	$\nu=0.03$	$\nu=0.05$	$\nu=0.01$	$\nu=0.03$	$\nu=0.05$	
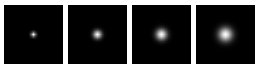	Bicubic	24.85	23.96	22.79	23.14	22.52	21.62	*23.15*
	RED	28.29	24.65	22.98	26.13	24.02	22.37	*24.74*
	IRCNN	27.43	26.22	25.86	26.12	25.11	24.79	*25.92*
	DPIR	28.62	27.30	26.47	**26.88**	25.96	25.22	*26.74*
	GS-PnP	**28.77**	**27.54**	**26.63**	26.85	**26.05**	**25.29**	***26.86***
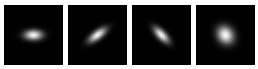	Bicubic	23.38	22.71	21.78	22.65	22.08	21.25	*22.31*
	RED	26.33	23.91	22.45	25.38	23.40	21.91	*23.90*
	IRCNN	25.83	24.89	24.59	25.36	24.36	23.95	*24.83*
	DPIR	**26.84**	25.59	24.89	**26.24**	24.98	**24.32**	*25.48*
	GS-PnP	26.80	**25.73**	**25.03**	26.18	**25.08**	24.31	***25.52***

Table 3: PSNR(dB) comparison of image super-resolution methods on CBSD10 with various scales s, blur kernels k and noise levels ν. PNSR results are averaged over kernels at each row. The best and second best results are respectively in bold and underlined.

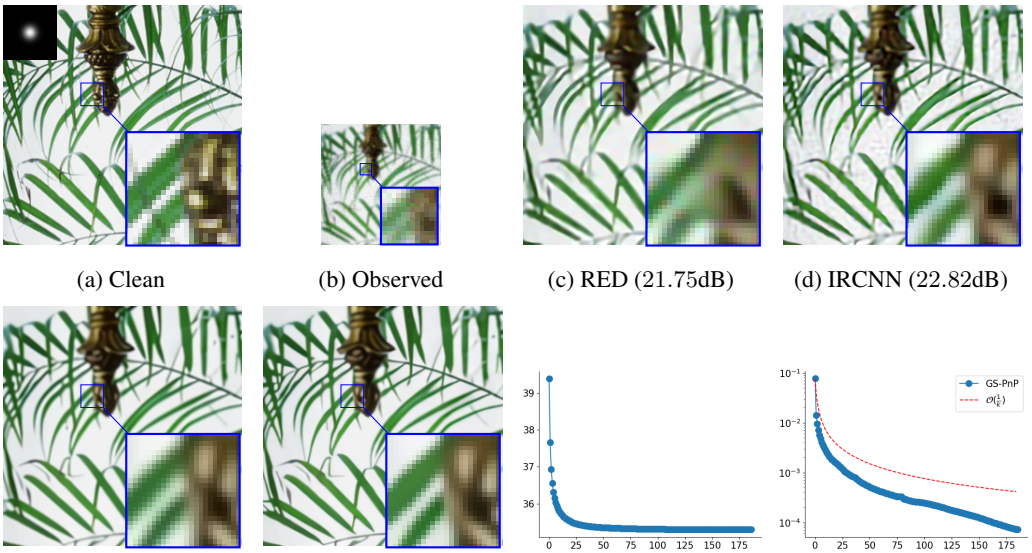

(a) Clean (b) Observed (c) RED (21.75dB) (d) IRCNN (22.82dB)

(e) DPIR (23.97dB) (f) GS-PnP (24.81dB) (g) $F(x_k)$ (h) γ_k (log scale)

Figure 2: Super-resolution with various methods on "leaves" (set3C) downsampled by 2, with the indicated blur kernel and input noise level $\nu = 0.03$. Note that our algorithm is the one that recovers sharpest leaves. In (g) and (h), we show the evolution of $F(x_k)$ and $\gamma_k = \min_{0\leq i\leq k} ||x_{i+1} - x_i||^2/||x_0||^2$ and in AppendixG.1 the evolution of the PSNR.. The empirical convergence rate is faster than the $\mathcal{O}(\frac{1}{k})$ theoretical worst case rate established in Remark 2.

6 Conclusion

In this work, we introduce a new PnP algorithm with convergence guarantees. A denoiser is trained to realize an exact gradient step on a regularization function that is formulated through a neural network. This denoiser is plugged in an iterative scheme closely related to PnP-HQS, which is proved to converge towards a stationary point of an explicit functional. One strength of this approach is to simultaneously allow for a non strongly convex (and not smooth) data-fidelity term with a denoiser that may not be non-expansive. Experiments conducted on ill-posed imaging problems (deblurring, super-resolution, inpainting) confirm the convergence results and show that the proposed PnP algorithm reaches state-of-the-art image restoration performance. This work also opens several research perspectives. One could first examine which information is encoded in the proposed prior. For example, based on the sharp visual results, one can question if a relation can be drawn between this prior and the gradient energy or sparsity. Also, it would be interesting to see if the recovery analysis developed in Liu et al. (2021) can adapt to the proposed framework.

7 REPRODUCIBILITY STATEMENT

Anonymous source code is given in supplementary material. It contains a README.md file that explains step by step how to run the algorithm and replicate the results of the paper. Moreover, the pseudocode of our algorithm is given Algorithm 1. In Section 5 it is precisely detailed how all the hyper-parameters are chosen and, for each experiment, which dataset is used. As for the theoretical results presented in Section 4, complete proofs are given in the appendixes.

8 ETHICS STATEMENT

We believe that this work does not raise potential ethical concerns.

REFERENCES

Eirikur Agustsson and Radu Timofte. Ntire 2017 challenge on single image super-resolution: Dataset and study. In *Proceedings of the IEEE conference on computer vision and pattern recognition workshops*, pp. 126–135, 2017.

Rizwan Ahmad, Charles A Bouman, Gregery T Buzzard, Stanley Chan, Sizhuo Liu, Edward T Reehorst, and Philip Schniter. Plug-and-play methods for magnetic resonance imaging: Using denoisers for image recovery. *IEEE signal processing magazine*, 37(1):105–116, 2020.

Hédy Attouch, Jérôme Bolte, Patrick Redont, and Antoine Soubeyran. Proximal alternating minimization and projection methods for nonconvex problems: An approach based on the kurdyka-łojasiewicz inequality. *Mathematics of operations research*, 35(2):438–457, 2010.

Hedy Attouch, Jérôme Bolte, and Benar Fux Svaiter. Convergence of descent methods for semi-algebraic and tame problems: proximal algorithms, forward–backward splitting, and regularized gauss–seidel methods. *Mathematical Programming*, 137(1-2):91–129, 2013.

H. H. Bauschke and P. L. Combettes. *Convex Analysis and Monotone Operator Theory in Hilbert Spaces*. Springer, 2011.

Amir Beck. *First-order methods in optimization*. SIAM, 2017.

Amir Beck and Marc Teboulle. Gradient-based algorithms with applications to signal recovery. *Convex optimization in signal processing and communications*, pp. 42–88, 2009.

Siavash A Bigdeli, Geng Lin, Tiziano Portenier, L Andrea Dunbar, and Matthias Zwicker. Learning generative models using denoising density estimators. *arXiv preprint arXiv:2001.02728*, 2020.

Siavash Arjomand Bigdeli and Matthias Zwicker. Image restoration using autoencoding priors. *arXiv preprint arXiv:1703.09964*, 2017.

Siavash Arjomand Bigdeli, Meiguang Jin, Paolo Favaro, and Matthias Zwicker. Deep mean-shift priors for image restoration. *arXiv preprint arXiv:1709.03749*, 2017.

Pakshal Bohra, Alexis Goujon, Dimitris Perdios, Sébastien Emery, and Michael Unser. Learning lipschitz-controlled activation functions in neural networks for plug-and-play image reconstruction methods. In *NeurIPS 2021 Workshop on Deep Learning and Inverse Problems*, 2021.

Jérôme Bolte, Aris Daniilidis, Olivier Ley, and Laurent Mazet. Characterizations of łojasiewicz inequalities: subgradient flows, talweg, convexity. *Transactions of the American Mathematical Society*, 362(6):3319–3363, 2010.

Gregery T Buzzard, Stanley H Chan, Suhas Sreehari, and Charles A Bouman. Plug-and-play unplugged: Optimization-free reconstruction using consensus equilibrium. *SIAM Journal on Imaging Sciences*, 11(3):2001–2020, 2018.

Stanley H Chan. Performance analysis of plug-and-play admm: A graph signal processing perspective. *IEEE Transactions on Computational Imaging*, 5(2):274–286, 2019.

Stanley H Chan, Xiran Wang, and Omar A Elgendy. Plug-and-play ADMM for image restoration: Fixed-point convergence and applications. *IEEE Transactions on Computational Imaging*, 3(1): 84–98, 2016.

Yunjin Chen and Thomas Pock. Trainable nonlinear reaction diffusion: A flexible framework for fast and effective image restoration. *IEEE transactions on pattern analysis and machine intelligence*, 39(6):1256–1272, 2016.

Regev Cohen, Michael Elad, and Peyman Milanfar. Regularization by denoising via fixed-point projection (RED-PRO). *SIAM Journal on Imaging Sciences*, 14(3):1374–1406, 2021.

P. L. Combettes and J.-C. Pesquet. Proximal splitting methods in signal processing. In *Fixed-Point Algorithms for Inverse Problems in Science and Engineering*, pp. 185–212. Springer, 2011.

Bradley Efron. Tweedie's formula and selection bias. *Journal of the American Statistical Association*, 106(496):1602–1614, 2011.

Ruturaj G Gavaskar and Kunal N Chaudhury. Plug-and-play ista converges with kernel denoisers. *IEEE Signal Processing Letters*, 27:610–614, 2020.

Ruturaj G Gavaskar, Chirayu D Athalye, and Kunal N Chaudhury. On plug-and-play regularization using linear denoisers. *IEEE Transactions on Image Processing*, 2021.

Ruturaj Girish Gavaskar and Kunal Narayan Chaudhury. On the proof of fixed-point convergence for plug-and-play ADMM. *IEEE Signal Processing Letters*, 26(12):1817–1821, 2019.

Donald Geman and Chengda Yang. Nonlinear image recovery with half-quadratic regularization. *IEEE transactions on Image Processing*, 4(7):932–946, 1995.

Mario González, Andrés Almansa, and Pauline Tan. Solving inverse problems by joint posterior maximization with autoencoding prior. *arXiv preprint arXiv:2103.01648*, 2021.

Bin Gu, De Wang, Zhouyuan Huo, and Heng Huang. Inexact proximal gradient methods for non-convex and non-smooth optimization. In *Proceedings of the AAAI Conference on Artificial Intelligence*, volume 32(1), 2018.

Johannes Hertrich, Sebastian Neumayer, and Gabriele Steidl. Convolutional proximal neural networks and plug-and-play algorithms. *Linear Algebra and its Applications*, 631:203–234, 2021.

Jonathan Ho, Ajay Jain, and Pieter Abbeel. Denoising diffusion probabilistic models. *arXiv preprint arXiv:2006.11239*, 2020.

Samuel Hurault, Thibaud Ehret, and Pablo Arias. Epll: an image denoising method using a gaussian mixture model learned on a large set of patches. *Image Processing On Line*, 8:465–489, 2018.

Zahra Kadkhodaie and Eero Peter Simoncelli. Solving linear inverse problems using the prior implicit in a denoiser. In *NeurIPS 2020 Workshop on Deep Learning and Inverse Problems*, 2020.

Rémi Laumont, Valentin De Bortoli, Andrés Almansa, Julie Delon, Alain Durmus, and Marcelo Pereyra. Bayesian imaging using plug & play priors: when langevin meets tweedie. *arXiv preprint arXiv:2103.04715*, 2021.

Anat Levin, Yair Weiss, Fredo Durand, and William T Freeman. Understanding and evaluating blind deconvolution algorithms. In *2009 IEEE Conference on Computer Vision and Pattern Recognition*, pp. 1964–1971. IEEE, 2009.

Huan Li and Zhouchen Lin. Accelerated proximal gradient methods for nonconvex programming. *Advances in neural information processing systems*, 28:379–387, 2015.

Bee Lim, Sanghyun Son, Heewon Kim, Seungjun Nah, and Kyoung Mu Lee. Enhanced deep residual networks for single image super-resolution. In *Proceedings of the IEEE conference on computer vision and pattern recognition workshops*, pp. 136–144, 2017.

Jiaming Liu, M Salman Asif, Brendt Wohlberg, and Ulugbek S Kamilov. Recovery analysis for plug-and-play priors using the restricted eigenvalue condition. *arXiv preprint arXiv:2106.03668*, 2021.

Sebastian Lunz, Ozan Öktem, and Carola-Bibiane Schönlieb. Adversarial regularizers in inverse problems. In *Proceedings of the 32nd International Conference on Neural Information Processing Systems*, pp. 8516–8525, 2018.

Kede Ma, Zhengfang Duanmu, Qingbo Wu, Zhou Wang, Hongwei Yong, Hongliang Li, and Lei Zhang. Waterloo Exploration Database: New challenges for image quality assessment models. *IEEE Transactions on Image Processing*, 26(2):1004–1016, Feb. 2017.

Stéphane Mallat. *A Wavelet Tour of Signal Processing, The Sparse Way*. Academic Press, Elsevier, 3rd edition edition, 2009. ISBN 978-0-12-374370-1.

D. Martin, C. Fowlkes, D. Tal, and J. Malik. A database of human segmented natural images and its application to evaluating segmentation algorithms and measuring ecological statistics. In *Proc. 8th Int'l Conf. Computer Vision*, volume 2, pp. 416–423, July 2001.

Tim Meinhardt, Michael Moller, Caner Hazirbas, and Daniel Cremers. Learning proximal operators: Using denoising networks for regularizing inverse imaging problems. In *Proceedings of the IEEE International Conference on Computer Vision*, pp. 1781–1790, 2017.

J.J. Moreau. Proximité et dualité dans un espace hilbertien. *Bulletin de la Société Mathématique de France*, 93:273–299, 1965. URL `http://eudml.org/doc/87067`.

Pravin Nair, Ruturaj Girish Gavaskar, and Kunal Narayan Chaudhury. Fixed-point and objective convergence of plug-and-play algorithms. *IEEE Transactions on Computational Imaging*, 2021.

Peter Ochs, Yunjin Chen, Thomas Brox, and Thomas Pock. ipiano: Inertial proximal algorithm for nonconvex optimization. *SIAM Journal on Imaging Sciences*, 7(2):1388–1419, 2014.

Jean-Christophe Pesquet, Audrey Repetti, Matthieu Terris, and Yves Wiaux. Learning maximally monotone operators for image recovery. *SIAM Journal on Imaging Sciences*, 14(3):1206–1237, 2021.

Jean Prost, Antoine Houdard, Andrés Almansa, and Nicolas Papadakis. Learning local regularization for variational image restoration. *arXiv preprint arXiv:2102.06155*, 2021.

Edward T Reehorst and Philip Schniter. Regularization by denoising: Clarifications and new interpretations. *IEEE transactions on computational imaging*, 5(1):52–67, 2018.

Yaniv Romano, Michael Elad, and Peyman Milanfar. The little engine that could: Regularization by denoising (red). *SIAM Journal on Imaging Sciences*, 10(4):1804–1844, 2017.

L. Rudin, S. Osher, and E. Fatemi. Nonlinear total variation based noise removal algorithms. *Phys. D*, 60:259–268, 1992.

Ernest Ryu, Jialin Liu, Sicheng Wang, Xiaohan Chen, Zhangyang Wang, and Wotao Yin. Plug-and-play methods provably converge with properly trained denoisers. In *International Conference on Machine Learning*, pp. 5546–5557. PMLR, 2019.

Tim Salimans and Jonathan Ho. Should ebms model the energy or the score? In *Energy Based Models Workshop-ICLR 2021*, 2021.

Saeed Saremi. On approximating ∇f with neural networks. *arXiv preprint arXiv:1910.12744*, 2019.

Saeed Saremi and Aapo Hyvarinen. Neural empirical bayes. *arXiv preprint arXiv:1903.02334*, 2019.

Suhas Sreehari, S Venkat Venkatakrishnan, Brendt Wohlberg, Gregery T Buzzard, Lawrence F Drummy, Jeffrey P Simmons, and Charles A Bouman. Plug-and-play priors for bright field electron tomography and sparse interpolation. *IEEE Transactions on Computational Imaging*, 2(4): 408–423, 2016.

Yu Sun, Brendt Wohlberg, and Ulugbek S Kamilov. An online plug-and-play algorithm for regularized image reconstruction. *IEEE Transactions on Computational Imaging*, 5(3):395–408, 2019.

Yu Sun, Zihui Wu, Xiaojian Xu, Brendt Wohlberg, and Ulugbek S Kamilov. Scalable plug-and-play admm with convergence guarantees. *IEEE Transactions on Computational Imaging*, 7:849–863, 2021.

Matthieu Terris, Audrey Repetti, Jean-Christophe Pesquet, and Yves Wiaux. Building firmly nonexpansive convolutional neural networks. In *ICASSP 2020-2020 IEEE International Conference on Acoustics, Speech and Signal Processing (ICASSP)*, pp. 8658–8662. IEEE, 2020.

Singanallur V Venkatakrishnan, Charles A Bouman, and Brendt Wohlberg. Plug-and-play priors for model based reconstruction. In *2013 IEEE Global Conference on Signal and Information Processing*, pp. 945–948. IEEE, 2013.

Kaixuan Wei, Angelica Aviles-Rivero, Jingwei Liang, Ying Fu, Carola-Bibiane Schönlieb, and Hua Huang. Tuning-free plug-and-play proximal algorithm for inverse imaging problems. In *International Conference on Machine Learning*, pp. 10158–10169. PMLR, 2020.

Xiaojian Xu, Yu Sun, Jiaming Liu, Brendt Wohlberg, and Ulugbek S Kamilov. Provable convergence of plug-and-play priors with mmse denoisers. *arXiv preprint arXiv:2005.07685*, 2020.

Xin Yuan, Yang Liu, Jinli Suo, and Qionghai Dai. Plug-and-play algorithms for large-scale snapshot compressive imaging. In *Proceedings of the IEEE/CVF Conference on Computer Vision and Pattern Recognition (CVPR)*, June 2020.

Kai Zhang, Wangmeng Zuo, Yunjin Chen, Deyu Meng, and Lei Zhang. Beyond a gaussian denoiser: Residual learning of deep cnn for image denoising. *IEEE Transactions on Image Processing*, 26 (7):3142–3155, 2017a.

Kai Zhang, Wangmeng Zuo, Shuhang Gu, and Lei Zhang. Learning deep cnn denoiser prior for image restoration. In *Proceedings of the IEEE conference on computer vision and pattern recognition*, pp. 3929–3938, 2017b.

Kai Zhang, Wangmeng Zuo, and Lei Zhang. Ffdnet: Toward a fast and flexible solution for cnn-based image denoising. *IEEE Transactions on Image Processing*, 27(9):4608–4622, 2018.

Kai Zhang, Yawei Li, Wangmeng Zuo, Lei Zhang, Luc Van Gool, and Radu Timofte. Plug-and-play image restoration with deep denoiser prior. *IEEE Transactions on Pattern Analysis and Machine Intelligence*, 2021.

Ningning Zhao, Qi Wei, Adrian Basarab, Nicolas Dobigeon, Denis Kouamé, and Jean-Yves Tourneret. Fast single image super-resolution using a new analytical solution for $\ell_2 - \ell_2$ problems. *IEEE Transactions on Image Processing*, 25(8):3683–3697, 2016.

Daniel Zoran and Yair Weiss. From learning models of natural image patches to whole image restoration. In *2011 International Conference on Computer Vision*, pp. 479–486. IEEE, 2011.

A Proof of Theorem 1

We first remind that a function $f : \mathbb{R}^n \longrightarrow \mathbb{R} \cup +\infty$ is proper if its domain

$$dom(f) = \{x \in \mathbb{R}, f(x) < +\infty\} \tag{15}$$

is non empty. Also, recall that f is lower semicontinuous at x^* if $\liminf_{x \to x^*} f(x) \geq f(x^*)$.

Proof.

(i) For ease of notation, we consider $\lambda = 1$. The generalisation for any $\lambda > 0$ is straightforward by rescaling g_σ (and L) accordingly. We denote the proximal gradient fixed point operator $T_\tau = \mathrm{Prox}_{\tau f} \circ (\mathrm{Id} - \tau \nabla_x g_\sigma)$, the objective function $F = f + g_\sigma$ and we introduce

$$Q_\tau(x, y) = g_\sigma(y) + \langle x - y, \nabla g_\sigma(y) \rangle + \frac{1}{2\tau} ||x - y||^2 + f(x). \tag{16}$$

We have

$$\begin{aligned}\arg\min_x Q_\tau(x,y) &= \arg\min_x g_\sigma(y) + \langle x-y, \nabla g_\sigma(y)\rangle + \frac{1}{2\tau}||x-y||^2 + f(x) \\ &= \arg\min_x f(x) + \frac{1}{2\tau}||x-(y-\tau\nabla g_\sigma(y)||^2 \\ &= \mathrm{Prox}_{\tau f}\circ(\mathrm{Id}-\tau\nabla_x g_\sigma)(y) = T_\tau(y)\end{aligned} \tag{17}$$

By definition for the $\arg\min$, $x_{k+1} = T_\tau(x_k) \Rightarrow Q_\tau(x_{k+1}, x_k) \leq Q_\tau(x_k, x_k)$. Moreover, with g_σ being L-smooth, we have by the descent lemma, for any $\tau \leq \frac{1}{L}$ and any $x, y \in \mathbb{R}^n$,

$$g_\sigma(x) \leq g_\sigma(y) + \langle x-y, \nabla g_\sigma(y)\rangle + \frac{1}{2\tau}||x-y||^2 \tag{18}$$

so that for every $x, y \in \mathbb{R}^n$,

$$Q_\tau(x,x) = F(x) \quad \text{and} \quad Q_\tau(x,y) \geq F(x) \tag{19}$$

Therefore, at iteration k,

$$F(x_{k+1}) \leq Q_\tau(x_{k+1}, x_k) \leq Q_\tau(x_k, x_k) = F(x_k) \tag{20}$$

$(F(x_k))$ is thus non-increasing. Since F is lower-bounded, $(F(x_k))$ thus converges to a limit F^*.

(ii) Note that $Q_\tau(x_{k+1}, x_k) \leq Q_\tau(x_k, x_k)$ implies

$$f(x_{k+1}) \leq f(x_k) - \langle x_{k+1}-x_k, \nabla g_\sigma(x_k)\rangle - \frac{1}{2\tau}||x_{k+1}-x_k||^2. \tag{21}$$

Using also (18) with stepsize $\frac{1}{L}$, we get

$$\begin{aligned}F(x_{k+1}) &= f(x_{k+1}) + g_\sigma(x_{k+1}) \\ &\leq f(x_k) - \langle x_{k+1}-x_k, \nabla g_\sigma(x_k)\rangle - \frac{1}{2\tau}||x_{k+1}-x_k||^2 \\ &+ g_\sigma(x_k) + \langle x_{k+1}-x_k, \nabla g_\sigma(x_k)\rangle + \frac{L}{2}||x_{k+1}-x_k||^2 \\ &= F(x_k) - \left(\frac{1}{2\tau} - \frac{L}{2}\right)||x_{k+1}-x_k||^2.\end{aligned} \tag{22}$$

Summing over $k = 0, 1, ..., m$ gives

$$\begin{aligned}\sum_{k=0}^{m} ||x_{k+1}-x_k||^2 &\leq \frac{1}{\frac{1}{2\tau}-\frac{L}{2}}\left(F(x_0) - F(x_{m+1})\right) \\ &\leq \frac{1}{\frac{1}{2\tau}-\frac{L}{2}}\left(F(x_0) - F^*\right).\end{aligned} \tag{23}$$

Therefore, $\lim_{k\to\infty} ||x_{k+1}-x_k|| = 0$.

(iii) We begin by the two following lemmas characterizing the proximal gradient descent operator $T_\tau = \mathrm{Prox}_{\tau f}\circ(\mathrm{Id}-\tau\nabla_x g_\sigma)$.

Lemma 1. *With the assumptions of Theorem 1, for $x^* \in \mathbb{R}^n$, x^* is a fixed point of the proximal gradient descent operator $T_\tau = \mathrm{Prox}_{\tau f}\circ(\mathrm{Id}-\tau\nabla_x g_\sigma)$,* i.e. *$T_\tau(x^*) = x^*$, if and only if x^* is a stationary point of problem (10),* i.e. $-\nabla g_\sigma(x^*) \in \partial f(x^*)$.

Proof. By definition of the proximal operator, we have

$$\begin{aligned}T_\tau(x^*) = x^* &\Leftrightarrow x^* = \mathrm{Prox}_{\tau f}\circ(\mathrm{Id}-\tau\nabla_x g_\sigma)(x^*) \\ &\Leftrightarrow x^* - \tau\nabla_x g_\sigma(x^*) - x^* \in \tau\partial f(x^*) \\ &\Leftrightarrow -\nabla_x g_\sigma(x^*) \in \partial f(x^*).\end{aligned} \tag{24}$$

□

Lemma 2. *With the assumptions of Theorem 1, T_τ is $1+\tau L$ Lipschitz.*

Proof. Using the fact that for f convex, $\mathrm{Prox}_{\tau f}$ is 1-Lipschitz ((Bauschke & Combettes, 2011, Proposition 12.28)), and by the Lipschitz property of $\nabla_x g_\sigma$

$$\begin{aligned} ||T_\tau(x) - T_\tau(y)|| &= ||\mathrm{Prox}_{\tau f} \circ (\mathrm{Id} - \tau \nabla_x g_\sigma)(x) - \mathrm{Prox}_{\tau f} \circ (\mathrm{Id} - \tau \nabla_x g_\sigma)(y)|| \\ &\leq ||(\mathrm{Id} - \tau \nabla_x g_\sigma)(x) - (\mathrm{Id} - \tau \nabla_x g_\sigma)(y)|| \\ &\leq (1+\tau L)||x-y||. \end{aligned} \tag{25}$$

□

Note that, by nonconvexity of g_σ, the fixed point operator T_τ is not necessarily non-expansive, but we can still show the convergence of the fixed-point algorithm towards a critical point of the objective function. We can now turn to the proof of (iii). Let x^* be a cluster point of $(x_k)_{k\geq 0}$. Then there exists a subsequence $(x_{k_j})_{j\geq 0}$ converging to x^*. We have $\forall j \geq 0$,

$$\begin{aligned} ||x^* - T_\tau(x^*)|| &\leq ||x^* - x_{k_j}|| + ||x_{k_j} - T_\tau(x_{k_j})|| + ||T_\tau(x_{k_j}) - T_\tau(x^*)|| \\ &\leq (2+\tau L)||x^* - x_{k_j}|| + ||x_{k_j} - T_\tau(x_{k_j})|| \text{ by Lemma 2.} \end{aligned} \tag{26}$$

Using (ii), the right-hand side of the inequity tends to 0 as $j \to \infty$. Thus $||x^* - T_\tau(x^*)|| = 0$ and $x^* = T_\tau(x^*)$, which by Lemma 1 means that x^* is a stationary point of problem (10). □

B On the boundedness of (x_k)

In order to obtain convergence of the iterates, in Theorem 2 the generated sequence (x_k) is assumed to be bounded. In the experiments (Section 5), we observed that under the rest of assumptions of Theorem 2, boundedness was always verified. A sufficient condition for the boundedness of the iterates is the coercivity of the objective function, that is, $\lim_{|x|\to\infty} F(x) = +\infty$ (because the non-increasing property gives $F(x_k) \leq F(x_0)$).

Similar to Laumont et al. (2021), we can constrain F to be coercive by choosing a convex compact set $C \subset \mathbb{R}^n$ where the iterates should stay and by adding an extra term to the regularization g_σ:

$$\hat{g}_\sigma(x) = g_\sigma(x) + \frac{1}{2}||x - \Pi_C(x)||^2 = \frac{1}{2}||x - N_\sigma(x)||^2 + \frac{1}{2}||x - \Pi_C(x)||^2 \tag{27}$$

with Π_C the Euclidian projection on C. As g_σ is differentiable, the gradient step becomes

$$(\mathrm{Id} - \tau\lambda \nabla_x \hat{g}_\sigma)(x) = (\mathrm{Id} - \tau\lambda \nabla_x g_\sigma) + \tau\lambda(x - \Pi_C(x)). \tag{28}$$

In our experiments, we choose the compact set C as $C = [-1, 2]^n$. In practice we observe that all the iterates always remain in C and that the extra regularization term $||x - \Pi_C(x)||^2$ is never activated. Therefore, we don't present this technical adaptation in Algorithm 1 but we let the reader aware that boundedness of (x_k) is not a limiting assumption.

C KL property

Definition 1. *Kurdyka-Lojasiewicz (KL) property (taken from Attouch et al. (2010))*

(a) A function $f : \mathbb{R}^n \longrightarrow \mathbb{R} \cup +\infty$ is said to have the Kurdyka-Lojasiewicz property at $x^* \in dom(f)$ if there exists $\eta \in (0, +\infty)$, a neighborhood U of x^* and a continuous concave function $\psi : [0, \eta) \longrightarrow \mathbb{R}_+$ such that $\psi(0) = 0$, ψ is $\mathcal{C}^1$ on $(0, \eta)$, $\psi' > 0$ on $(0, \eta)$ and $\forall x \in U \cap [f(x^*) < f < f(x^*) + \eta]$, the Kurdyka-Lojasiewicz inequality holds :

$$\psi'(f(x) - f(x^*)) dist(0, \partial f(x)) \geq 1 \tag{29}$$

(b) Proper lower semicontinuous functions which satisfy the Kurdyka-Lojasiewicz inequality at each point of $dom\partial f$ are called KL functions.

This condition can be interpreted as the fact that, up to a reparameterization, the function is sharp *i.e.* we can bound its subgradients away from 0. A big class of functions that have the KL-property is given by real semi-algebraic functions. For more details and interpretations, we refer to Attouch et al. (2010) and Bolte et al. (2010).

D LIPSCHITZ CONSTANT OF ∇g_σ

First, let us give a result which ensures that a large class of neural networks trained with differentiable activation functions have Lipschitz gradients with respect to the input image.

Proposition 2. *Let $H = h_p \circ \ldots \circ h_1$ be a composition of differentiable functions $h_i : \mathbb{R}^{d_{i-1}} \to \mathbb{R}^{d_i}$. Let us assume that for any i the differential map h_i' is bounded and Lipschitz. Then H' is Lipschitz.*

Proof. Let us denote $H_i = h_i \circ \ldots \circ h_1$ (and by convention, $H_0 = \mathsf{Id}$). Let $\|h_i'\|_\infty$ be the best uniform bound on the operator norms $\|h_i'(x)\|, x \in \mathbb{R}^{d_{i-1}}$ (which is also the best Lipschitz constant of h_i). Let us also denote $\|h_i'\|_{\text{Lip}}$ the Lipschitz constant of h_i'. The chain rule gives that for any x, $H'(x)$ can be expressed as a composition of linear maps

$$H'(x) = h_p'(H_{p-1}(x))h_{p-1}'(H_{p-2}(x)) \ldots h_1'(x) \tag{30}$$

Therefore, for any x, y,

$$H'(x) - H'(y) = \sum_{i=0}^{p-1} h_p'(H_{p-1}(x)) \ldots h_{i+2}'(H_{i+1}(x))h_{i+1}'(H_i(x))h_i'(H_{i-1}(y)) \ldots h_1'(y) \tag{31}$$

$$- h_p'(H_{p-1}(x)) \ldots h_{i+2}'(H_{i+1}(x))h_{i+1}'(H_i(y))h_i'(H_{i-1}(y)) \ldots h_1'(y). \tag{32}$$

We can thus bound the operator norms

$$\|H'(x) - H'(y)\| \leq \sum_{i=0}^{p-1} \Big(\|h_p'(H_{p-1}(x)) \ldots h_{i+2}'(H_{i+1}(x))\| \tag{33}$$

$$\|h_{i+1}'(H_i(x)) - h_{i+1}'(H_i(y))\| \|h_i'(H_{i-1}(y)) \ldots h_1'(y)\| \Big). \tag{34}$$

and thus

$$\|H'(x) - H'(y)\| \leq \sum_{i=0}^{p-1} \Big(\prod_{j \neq i+1} \|h_j'\|_\infty \Big) \|h_{i+1}'\|_{\text{Lip}} \|H_i'\|_\infty \|x - y\| \tag{35}$$

which concludes because the chain-rule ensures that $\|H_i'\|_\infty \leq \|h_i'\|_\infty \ldots \|h_1'\|_\infty$. □

Proposition 2 applies for a neural network obtained as a composition of fully-connected layers with ELU activation functions, that is, by composing functions of the form

$$h(x) = E(Ax + b) \tag{36}$$

where A is a matrix, b a vector and E is the element-wise ELU defined by

$$E(x)_i = \begin{cases} x_i & \text{if } x_i \geq 0 \\ e^{x_i} - 1 & \text{if } x_i < 0 \,. \end{cases} \tag{37}$$

It is easy to see that E is differentiable and that E' is 1-Lipschitz and $\|E'\|_\infty \leq 1$. Therefore

$$h'(x) = E'(Ax + b)A \tag{38}$$

is also bounded and Lipschitz.

Let us also mention that this proposition encompasses the case of U-nets which, in addition to composing fully-connected layers, also integrates skip-connections. For example, taking a skip-connection on a composition $h_3 \circ h_2 \circ h_1$ amounts to defining

$$H(x) = h_3\big(\, h_2(h_1(x)) \, , \, h_1(x) \, \big). \tag{39}$$

This can be simply rewritten $H = h_3 \circ \tilde{h}_2 \circ h_1$ where

$$\tilde{h}_2(x) = \big(h_2(h_1(x)), h_1(x)\big). \tag{40}$$

It is then clear that $\tilde{h}_2$ has bounded Lipschitz differential as soon as h_1 and h_2 do.

The bound obtained in the proof of Proposition 2 is exponential in the depth of the neural network. We now provide some experiments showing that, in practice, the Lipschitz constant of ∇g_σ does not explode. With the parameterization proposed in equation (5), g_σ is twice differentiable with the right choice of the activation functions in the CNN N_σ (*e.g.* ELU). We show in Figure 3, for various noise levels σ, the distribution of $||\nabla^2 g_\sigma(x)||_S$ on the training image set X, estimated with power iterations. The computed value varies a lot across images. Hence approximating the Lipschitz constant of ∇g_σ with $L = \max_{x \in X} ||\nabla^2 g_\sigma(x)||_S$ would lead to under-estimated stepsizes and slow convergence on most images. Backtracking solves this issue by finding at each iteration the optimal stepsize allowing sufficient decrease of the objective function.

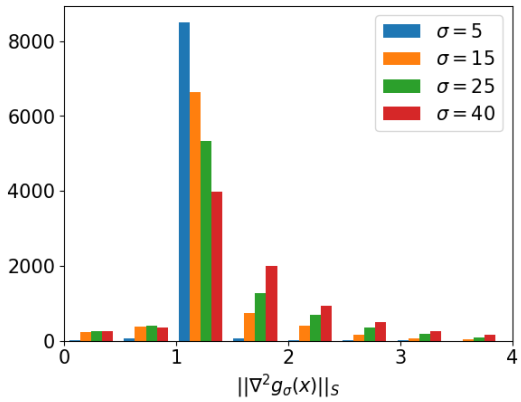

Figure 3: Histogram of the values of $||\nabla^2 g_\sigma(x)||_S$ evaluated on 128×128 images from the training dataset, degraded with white Gaussian noise with various standard deviations σ (./255). Figure best seen in color.

E Proof of Proposition 1

Proof. For a given stepsize τ, we showed in Appendix A, equation (22) that

$$F(x_k) - F(T_\tau(x_k)) \geq \frac{1}{2}\left(\frac{1}{\tau} - L\right)||T_\tau(x_k) - x_k||^2. \tag{41}$$

Taking $\tau < \frac{1-2\gamma}{L}$, we get $\frac{1}{2}(\frac{1}{\tau} - L) > \frac{\gamma}{\tau}$ so that

$$F(x_k) - F(T_\tau(x_k)) > \frac{\gamma}{\tau}||T_\tau(x_k) - x_k||^2. \tag{42}$$

Hence, when $\tau < \frac{1-2\gamma}{L}$, the sufficient decrease condition equation (42) is satisfied and the backtracking procedure ($\tau \longleftarrow \eta\tau$) must end.

In the proof of Theorem 1, we can replace the sufficient decrease (22) by (42) and finish the proof with the same arguments. In the same way, in the proof of Theorem 2 given in Attouch et al. (2013)[Theorem 5.1], our sufficient decrease (42) replaces Attouch et al. (2013, Equation (52)).

□

F Expansiveness of the denoiser

As g_σ is not necessarily convex, our GS-DRUNet denoiser $D_\sigma = \mathrm{Id} - \nabla g_\sigma$ is not necessarily non-expansive and neither is the gradient step $\mathrm{Id} - \lambda\tau\nabla g_\sigma$. This is not an issue as, unlike previous theoretical PnP studies (Terris et al., 2020; Reehorst & Schniter, 2018), our convergence results do not require a non-expansive denoising step. To advocate that our method converges without this assumption, we show in Figure 4 the evolution of $\frac{||D_\sigma(x_{k+1}) - D_\sigma(x_k)||}{||x_{k+1} - x_k||}$ along the algorithm that was run to obtain the super-resolution results of Figure 7. In this experiment, backtracking did not get

activated and stayed fixed at $\lambda\tau = 1$. The gradient step in the PGD algorithm was thus simply a denoising step $D_\sigma = \mathrm{Id} - \lambda\tau\nabla g_\sigma$. Note that the Lipschitz constant of D_σ goes above 1 but convergence is still observed as shown by the two convergence curves in Figure 7.

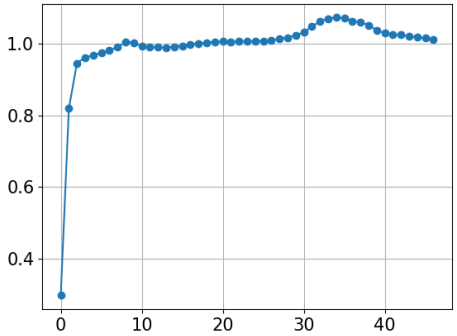

Figure 4: Lipschitz constant of D_σ along the iterates of the algorithm when performing the super-resolution experiments presented Figure 7. Note that the Lipschitz constant goes above 1 *i.e.* it is not non-expansive, but we still empirically verified convergence (see convergence curves Figure 7).

G Additional Experiments

G.1 PSNR convergence curves

We first plot Figure 5 the evolution of the PSNR along the iterations of the PnP algorithm during the experiments of Figure 1 and Figure 2. This illustrates that the minimization of F coincides with the maximization of the PSNR, which supports the interest of the optimized functional $F = f + \lambda g_\sigma$.

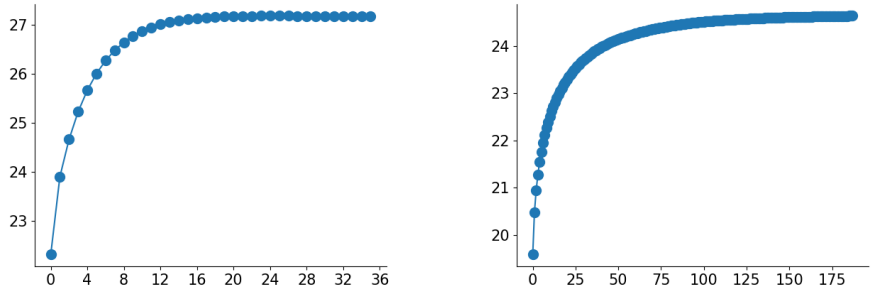

(a) Deblurring

(b) Super-resolution

Figure 5: Evolution of the PSNR along the iterations of the algorithm, during (a) the deblurring experiment of Figure 1 and (b) the super-resolution experiment of Figure 2. Note that the convergence in PSNR follows the convergence in function value (represented Figures 1(g) and 2(g)).

G.2 Deblurring

We give here additional image deblurring experiments. We first present the PSNR performance comparison on the Set3c dataset in Table 4. We also provide an evaluation of the 3 best methods (GS-PnP, DPIR and IRCNN) on the full CBSD68 dataset in Table 5. For fair comparison with RED, we also expose Table 6 the PSNR calculated on the Y channel only. An additional visual comparison is finally shown in Figure 6. Details and comments are given in the corresponding captions.

ν	Method	(a)	(b)	(c)	(d)	(e)	(f)	(g)	(h)	(i)	(j)	*Avg*
0.01	EPLL	23.83	24.14	24.83	19.85	26.08	21.77	21.53	21.57	22.43	21.36	*22.74*
	RED	29.21	28.58	29.52	24.54	30.45	25.34	26.06	26.07	25.11	28.50	*27.34*
	IRCNN	33.36	33.06	33.11	32.87	34.24	34.08	33.25	32.87	27.78	29.67	*32.45*
	MMO	32.84	32.29	32.76	31.85	34.08	33.76	33.11	32.38	26.31	29.91	*31.93*
	DPIR	**34.94**	**34.46**	**34.25**	**34.34**	**35.57**	**35.53**	**34.49**	**34.21**	28.14	29.63	***33.56***
	GS-PnP	34.58	34.13	34.04	33.93	35.45	35.25	34.30	33.97	**28.16**	**29.78**	*33.34*
0.03	EPLL	21.21	21.10	22.65	18.78	24.12	20.77	20.42	19.89	20.61	20.60	*21.02*
	RED	25.42	24.89	25.69	22.67	26.86	23.84	24.06	23.87	21.49	25.45	*24.43*
	IRCNN	29.08	28.62	29.03	28.46	30.51	30.06	29.23	28.74	24.39	27.39	*28.55*
	DPIR	**30.33**	29.74	29.87	**29.67**	31.27	31.08	30.21	29.72	25.02	27.84	*29.48*
	GS-PnP	30.29	**29.84**	**30.14**	29.58	**31.53**	**31.24**	**30.41**	**29.96**	**26.13**	**28.56**	***29.77***
0.05	EPLL	19.84	19.60	21.40	17.71	22.77	19.68	19.02	18.24	19.81	20.12	*19.82*
	RED	21.93	21.27	22.79	20.32	24.01	22.05	22.06	21.41	19.79	23.21	*21.88*
	IRCNN	26.85	26.33	27.04	26.10	28.46	27.90	27.05	26.56	22.90	26.16	*26.54*
	DPIR	27.96	27.37	28.07	27.44	29.42	29.04	28.32	27.56	23.57	26.93	*27.57*
	GS-PnP	**28.08**	**27.75**	**28.35**	**27.56**	**29.60**	**29.17**	**28.49**	**28.01**	**24.67**	**27.47**	***27.91***

Table 4: PSNR(dB) comparison of image deblurring methods on set3C with various blur kernels k and noise levels ν. Best and second best results are displayed in bold and underlined. Similar to Table 2, for all kinds of kernels, the proposed method outperforms all competing methods at noise levels 0.03 and 0.05 and follows DPIR at lower noise level 0.01.

ν	Method	(a)	(b)	(c)	(d)	(e)	(f)	(g)	(h)	(i)	(j)	*Avg*
0.01	IRCNN	32.47	32.14	31.94	31.97	32.94	33.13	31.92	31.62	27.57	**28.45**	*31.42*
	DPIR	**33.26**	**32.82**	**32.48**	**32.65**	**33.57**	**33.85**	**32.49**	**32.22**	**27.65**	28.26	***31.93***
	GS-PnP	32.95	32.54	32.26	32.31	33.41	33.71	32.29	31.92	27.43	28.17	*31.70*
0.03	IRCNN	28.43	28.11	28.28	27.87	29.42	29.21	28.37	27.97	25.52	26.96	*28.01*
	DPIR	**28.88**	**28.53**	**28.55**	**28.30**	29.58	**29.62**	**28.69**	28.28	25.60	26.96	***28.30***
	GS-PnP	28.64	28.32	**28.55**	28.06	**29.71**	29.60	**28.69**	**28.31**	**25.79**	**27.10**	*28.28*
0.05	IRCNN	26.73	26.42	26.73	26.13	27.69	27.39	26.69	26.33	24.68	26.18	*26.40*
	DPIR	**27.04**	**26.80**	**27.07**	**26.53**	28.00	27.85	27.17	26.72	24.75	26.32	*26.82*
	GS-PnP	26.93	26.72	**27.07**	26.45	**28.09**	**27.87**	**27.21**	**26.82**	**25.02**	**26.45**	***26.86***

Table 5: PSNR(dB) performance of the fastest method (IRCNN/DPIR/GS-PnP) for image deblurring on the full CBSD68 dataset with various blur kernels k and noise levels ν, in the same conditions as Table 2. On CBSD10 (Table 2) or on CBSD68 (Table 5), we observed very similar performance gaps between the compared methods, which confirms that CBSD10 is large enough to compare accurately the PnP methods.

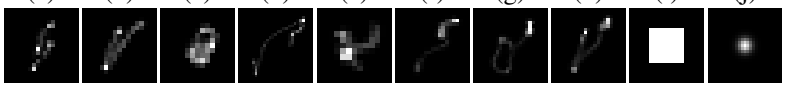

ν	Method	(a)	(b)	(c)	(d)	(e)	(f)	(g)	(h)	(i)	(j)	*Avg*
$\sqrt{2}/255$	RED$_Y$	35.19	34.78	34.58	34.64	35.49	35.65	34.70	34.37	**30.15**	**31.15**	*34.07*
	GS-PnP$_Y$	**36.20**	**35.76**	**35.21**	**35.55**	**36.33**	**36.87**	**35.16**	**34.79**	29.21	29.48	***34.45***
0.01	RED$_Y$	33.52	33.20	**33.20**	33.05	34.20	34.21	**33.22**	**32.90**	**28.77**	**30.44**	***32.67***
	GS-PnP$_Y$	**33.88**	**33.39**	33.15	**33.15**	**34.35**	**34.58**	**33.22**	32.81	28.23	29.12	*32.59*
0.03	RED$_Y$	29.26	28.83	29.28	28.53	**30.64**	**30.48**	29.50	29.06	26.18	**28.78**	***29.05***
	GS-PnP$_Y$	**29.45**	**29.11**	**29.39**	**28.82**	30.55	30.46	**29.55**	**29.14**	**26.50**	28.02	*29.01*
0.05	RED$_Y$	26.91	26.54	27.52	26.23	28.68	28.25	27.67	27.07	25.36	**27.98**	*27.22*
	GS-PnP$_Y$	**27.65**	**27.48**	**27.88**	**27.19**	**28.90**	**28.67**	**28.03**	**27.59**	**25.62**	27.29	***27.63***

Table 6: PSNR(dB) performance, evaluated on the luminance channel in YcbCr color space, of RED and GS-PnP for image deblurring on CBSD10. Remind that our method treats the RGB image as a whole before being evaluated on the Y channel while RED treats the Y channel independently. Compared to Table 2, we add the case $\nu = \sqrt{2}/255$ as in RED original paper (Romano et al. (2017)). Note that RED was optimized for kernels (i) and (j) and $\nu = \sqrt{2}/255$, and outperforms our method in this set of conditions. However, over the variety of kernels and noise levels, and in particular for motion blur, our method generally outperforms RED.

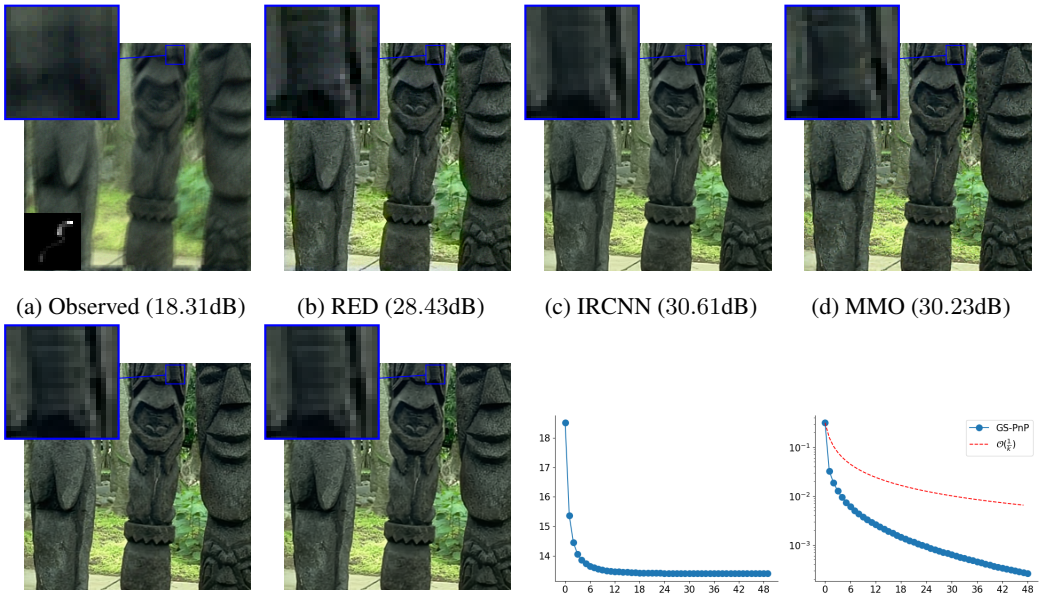

(a) Observed (18.31dB) (b) RED (28.43dB) (c) IRCNN (30.61dB) (d) MMO (30.23dB)

(e) DPIR (30.85dB) (f) GS-PnP (30.74dB) (g) $F(x_k)$ (h) γ_k (log scale)

Figure 6: Deblurring with various methods of an image from CSBD10 degraded with the indicated blur kernel and input noise level $\nu = 0.01$. In (g) and (h), we show the evolution of $F(x_k)$ and $\gamma_k = \min_{0 \leq i \leq k} ||x_{i+1} - x_i||^2 / ||x_0||^2$ along our algorithm. Note that GS-PnP and DPIR both recover fine textures while other methods tend to smooth details.

G.3 SUPER-RESOLUTION

We also present additional super-resolution experiments. We realize a full PSNR performance comparison on the Set3c dataset Table 7. We show additional visual comparisons between methods Figure 7 and Figure 8. Details and comments are given in the corresponding captions.

Kernels	Method	$s = 2$			$s = 3$			*Avg*
		$\nu = 0.01$	$\nu = 0.03$	$\nu = 0.05$	$\nu = 0.01$	$\nu = 0.03$	$\nu = 0.05$	
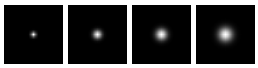	Bicubic	21.92	21.54	20.90	19.76	19.53	19.11	*20.46*
	RED	28.22	25.62	23.61	24.91	23.38	21.82	*24.59*
	IRCNN	28.35	26.40	25.27	25.61	24.45	23.37	*25.58*
	DPIR	29.08	27.27	26.21	**26.55**	25.33	24.41	*26.48*
	GS-PnP	**29.24**	**28.03**	**26.65**	25.90	**25.56**	**24.60**	***27.00***
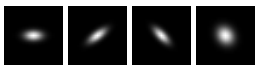	Bicubic	19.82	19.58	19.16	18.95	18.76	18.40	*19.11*
	RED	24.72	22.55	21.10	22.82	21.64	20.19	*22.17*
	IRCNN	25.10	23.44	22.52	24.25	22.60	21.58	*23.25*
	DPIR	**26.22**	24.52	23.56	**25.34**	23.57	22.50	***24.29***
	GS-PnP	25.45	**24.84**	**23.80**	24.53	**23.73**	**22.71**	*24.18*

Table 7: PSNR(dB) comparison of image super-resolution methods on set3C with various scales s, blur kernels k and noise levels ν. Similar to Table 3, for isotropic and anisotropic kernels, the proposed method outperforms all competing methods at noise levels 0.03 and 0.05 and follows DPIR at lower noise level 0.01.

Kernels	Method	$s = 2$			$s = 3$			*Avg*
		$\nu = 0.01$	$\nu = 0.03$	$\nu = 0.05$	$\nu = 0.01$	$\nu = 0.03$	$\nu = 0.05$	
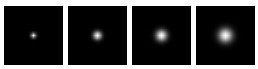	IRCNN	26.97	25.86	25.45	25.60	24.72	24.38	*25.50*
	DPIR	27.79	26.58	25.83	**26.05**	25.27	24.66	*26.03*
	GS-PnP	**27.88**	**26.81**	**26.01**	25.97	**25.35**	**24.74**	***26.13***
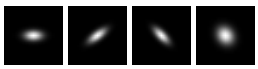	IRCNN	25.41	24.52	24.18	24.94	24.04	23.61	*24.45*
	DPIR	**26.08**	24.99	24.39	**25.53**	24.46	23.80	*24.88*
	GS-PnP	25.98	**25.07**	**24.53**	25.47	**24.56**	**23.92**	***24.92***

Table 8: PSNR(dB) performance of the fastest method (IRCNN/DPIR/GS-PnP) for image super-resolution on the full CBSD68 dataset with various blur kernels k and noise levels ν, in the same conditions as Table 3. Once again, on CBSD10 (Table 2) or on CBSD68 (Table 5), we observed very similar performance gaps between the compared methods, which again confirms that CBSD10 is large enough to compare accurately the PnP methods.

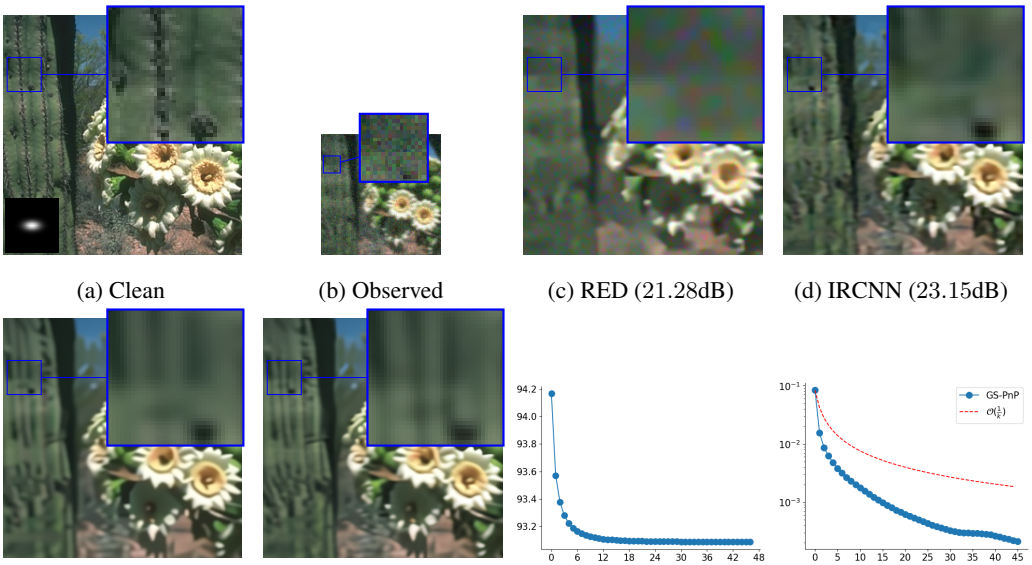

(a) Clean (b) Observed (c) RED (21.28dB) (d) IRCNN (23.15dB)

(e) DPIR (23.33dB) (f) GS-PnP (23.47dB) (g) $F(x_k)$ (h) γ_k (log scale)

Figure 7: Super-resolution with various methods on a CBSD10 image degraded with the indicated blur kernel, $s = 2$ and input noise level $\nu = 0.05$. In (g) and (h), we show the evolution of $F(x_k)$ and $\gamma_k = \min_{0 \leq i \leq k} ||x_{i+1} - x_i||^2 / ||x_0||^2$ along our algorithm. One can notice that the proposed method GS-PnP manages to extract more structure in the zoomed area than the competing methods

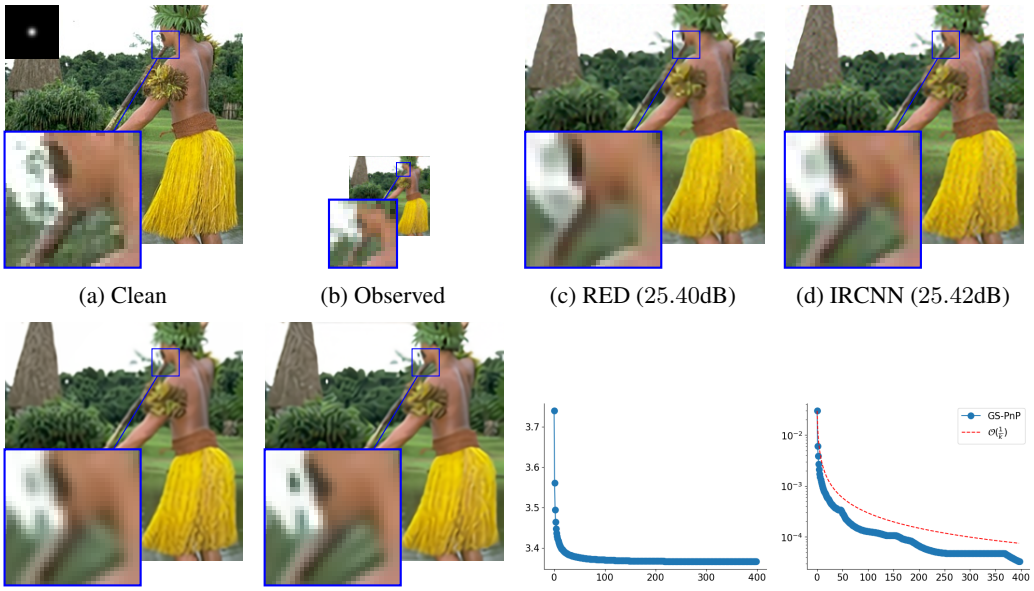

(a) Clean (b) Observed (c) RED (25.40dB) (d) IRCNN (25.42dB)

(e) DPIR (25.41dB) (f) GS-PnP (25.46dB) (g) $F(x_k)$ (h) γ_k (log scale)

Figure 8: Super-resolution with various methods on a CBSD10 image degraded with the indicated blur kernel, $s = 3$ and input noise level $\nu = 0.01$. In (g) and (h), we show the evolution of $F(x_k)$ and $\gamma_k = \min_{0 \leq i \leq k} ||x_{i+1} - x_i||^2 / ||x_0||^2$ along our algorithm.

G.4 INPAINTING (WITH NON-DIFFERENTIABLE DATA-FIDELITY TERM)

We now propose to apply our PnP scheme to image inpainting with the degradation model

$$y = Ax \tag{43}$$

where A is a diagonal matrix with values in $\{0, 1\}$. For inpainting, no noise is added to the degraded image. In this context, the data-fidelity term is the indicator function of $A^{-1}(\{y\}) = \{x \mid Ax = y\}$: $f(x) = \imath_{A^{-1}(\{y\})}$ (which, by definition, equals $+\infty$ on $A^{-1}(\{y\})$ and 0 elsewhere). Despite being non differentiable, f still verifies the assumptions of Theorems 1 and 2 and convergence is theoretically ensured. The proximal map becomes the orthogonal projection $\Pi_{A^{-1}(\{y\})}$

$$\mathrm{Prox}_{\tau f}(x) = \Pi_{A^{-1}(\{y\})}(x) = Ay - Ax + x \tag{44}$$

In our experiments, the diagonal of A is filled with Bernoulli random variables with parameter $p = 0.5$. We run our PnP algorithm with $\sigma = 10/255$. Given the form of f, we do not use the backtracking strategy and keep a fixed stepsize. Even if we do not exactly know the Lipschitz constant of ∇g_σ, we observed in Figure 4 that, for small noise, it was almost always estimated as slightly larger than 1. We thus choose $\lambda\tau = 1$ and empirically confirm convergence with this choice in follow-up experiments (see Figure 9). The algorithm is initialized with $x_0 = y + 0.5 * (\mathrm{Id} - A)y$ (masked pixels with value 0.5) and terminates when the number of iterations exceeds $K = 100$. We found it useful to run the first 10 iterations of the algorithm at larger noise level $\sigma = 50/255$. As y does not have noise, we found preferable not to run the last extra gradient pass from Algorithm 1.

We show inpainting results on set3C images Figure 9. Our PnP restores the input images with high accuracy, including its small details. Furthermore, convergence of the residual at rate $\mathcal{O}(\frac{1}{k})$ is empirically confirmed.

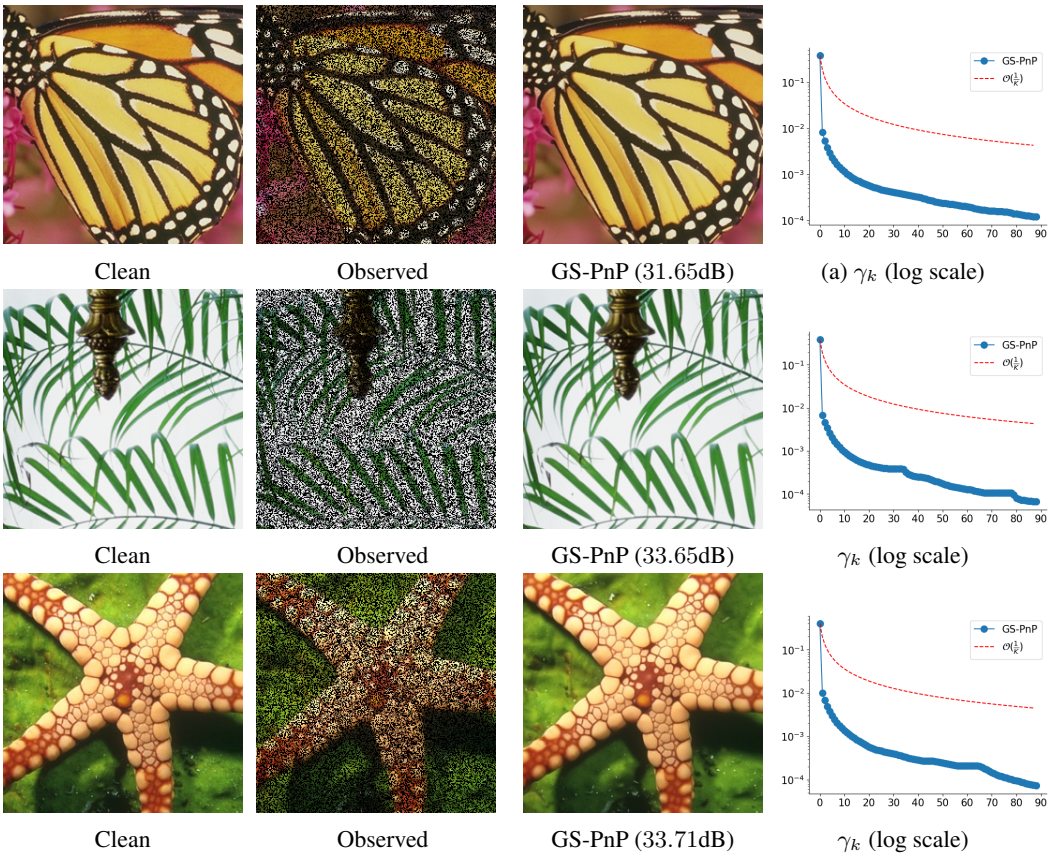

Figure 9: Inpainting results on set3C with pixels randomly masked with probability $p = 0.5$. In the last colomn, we show the evolution of $\gamma_k = \min_{0 \leq i \leq k} ||x_{i+1} - x_i||^2 / ||x_0||^2$ along the iterations.

G.5 INFLUENCE OF THE PARAMETERS

In this section we study more deeply the influence of the parameters involved in the GS-PnP algorithm. Figure 10 and Figure 11 respectively plot the average PSNR when deblurring the CBSD10 images with different values λ_ν and σ/ν, and fixed $\nu = 0.03$. Both parameters control the strength of the regularization. We observe that λ_ν and σ have a similar influence on the output: for small λ_ν or small σ, the regularization involved by the denoising pass is not sufficient to counteract the noise amplification done by the proximal steps with large τ (recall that when $\tau \to \infty$, $\mathrm{Prox}_{\tau f}$ tends to the pseudo-inverse of A). On the contrary, as expected, increasing λ and σ tends to over-smooth the output result.

On a single image, we also vary the main parameters of both GS-PnP and RED (Figure 12). For fair comparison, the PSNR is computed on the luminance channel only. This experiment confirms that, when manually optimizing the parameters for both methods, the PSNR results obtained with GS-PnP and RED remain close, as already observed in Table 6.

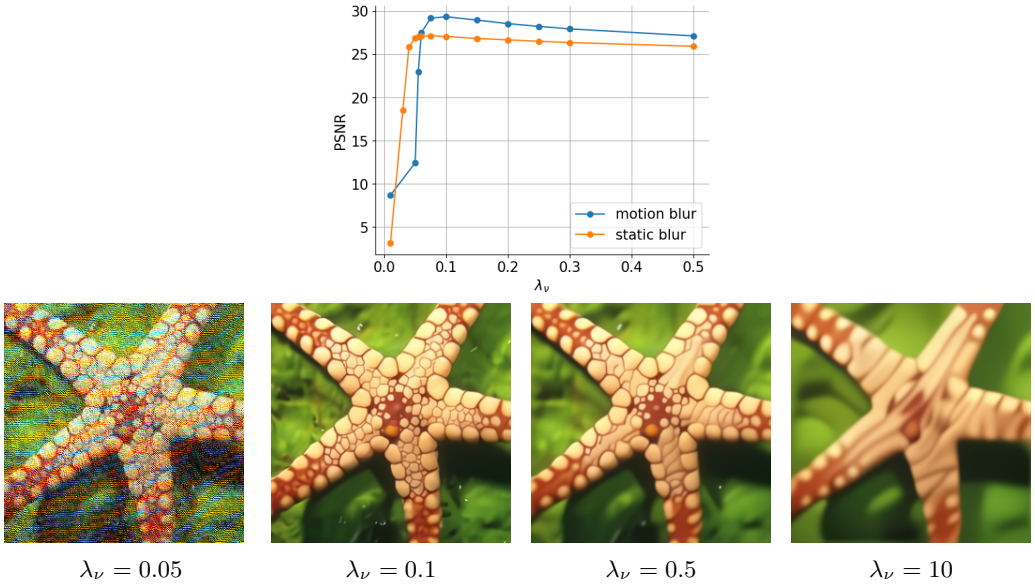

Figure 10: Influence of the choice of the parameter λ_ν for deblurring. Top: average PSNR when deblurring the images of CBSD10, blurred with the 8 motion blurs or the 2 static blurs, along with values of λ_ν. The other parameters remain unchanged. Bottom: visual results when deblurring "starfish" with various λ_ν (in the same conditions as Figure 1).

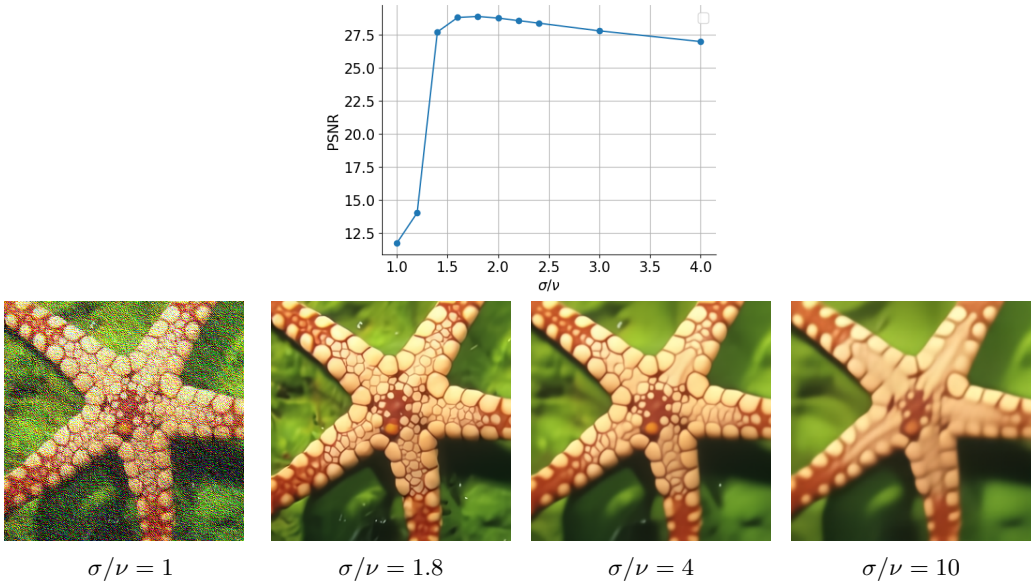

Figure 11: Influence of the choice of the parameter σ for deblurring. Top: average PSNR when deblurring the images of CBSD10, blurred with the 10 kernels, along with values of σ/ν, with $\nu = 0.03$. The other parameters remain unchanged. Bottom: visual results when deblurring "starfish" with various σ/ν, with $\nu = 0.03$ (in the same conditions as Figure 1).

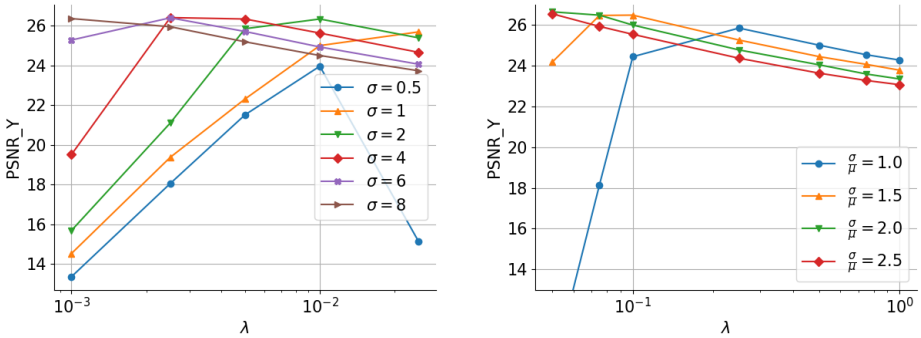

(a) RED

(b) GSPnP

Figure 12: Influence of the parameters σ and λ for RED and GS-PnP when deblurring the single image "starfish" degraded with uniform kernel and $\nu = 7.65/255$. For fair comparison, like in Table 6, the PSNR is calculated on the Y channel only. Remember that the results of Table 6 were obtained with $\sigma = 3.25, \lambda = 0.02$ for RED and $\sigma = 2\nu, \lambda = 0.075$ for GS-PnP.

G.6 INFLUENCE OF THE INITIALIZATION

In Figure 13, we examines the robustness of the method to the initialization. As can be seen on this experiment, the output image does not change much even for relatively large perturbation of the initialization. We thus observe a robustness to the initialization, both in terms of visual aspect and PSNR. We also observed that initializing with a uniform image does not change the output of the algorithm. We suggest that the robustness to the initialization comes from the first proximal steps on the data-fidelity term (with a large τ), which prevents the algorithm to be stuck in a poor local minimum. Note that it is the backtracking procedure that allows to use large τ in the beginning of the algorithm.

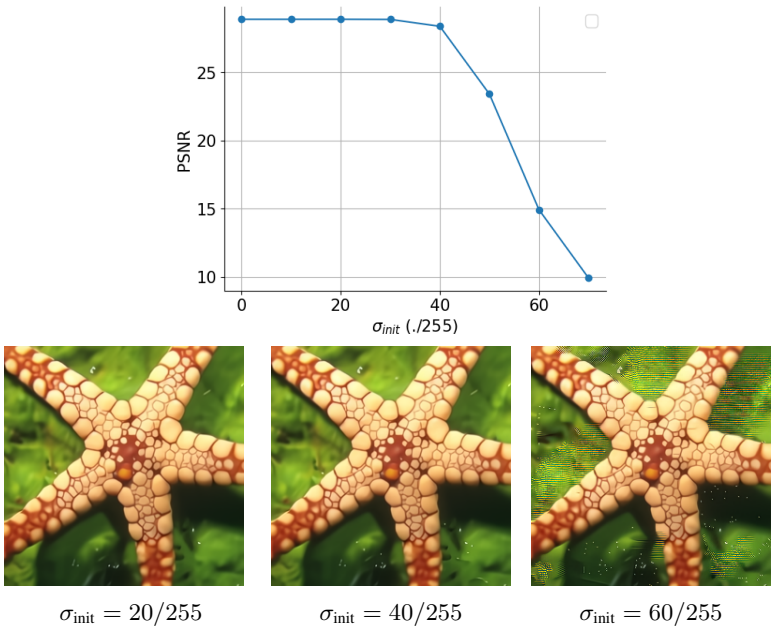

Figure 13: Influence of the initialitation z_0 on the deblurring result. Instead of initializing with the blurred image $z_0 = y$ as done in Section 5.2.1, we set $z_0 = y + \xi_{\sigma_{\text{init}}}$ with $\xi_{\sigma_{\text{init}}}$ an AWGN with standard deviation σ_{init}. By increasing the noise level σ_{init}, we investigate the robustness of the result to changes in the initialization of the algorithm. Top: PSNR values, along with values of σ_{init} Bottom: corresponding visual results on "starfish" with various σ_{init} (in the same conditions as Figure 1). We observe that the algorithm is robust to noisy initializations up to a relatively large value of σ_{init}.

H DRUNET *light* ARCHITECTURE

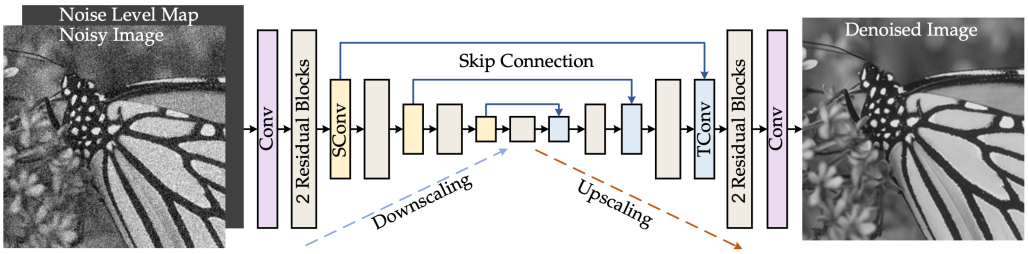

Figure 14: Architecture of the DRUNet *light* denoiser (Zhang et al. (2021)) used to parametrize N_σ.